









Thermal energy confinement time of spherical tokamak plasmas in PI3

A. Tancetti* , C. Ribeiro , S.J. Howard, S. Coop , C.P. McNally , M. Reynolds , P. Kholodov, F. Braglia, R. Zindler, C. Macdonald, E. Love, P. Carle, X. Feng , A. Rohollahi , K. Leci, D. Plant, C. Dunlea , R. Ivanov and A. Mossman

General Fusion Inc., 6020 Russ Baker Way, Richmond, BC V7B 1B4, Canada

E-mail: andrea.tancetti@generalfusion.com

Received 22 August 2024, revised 26 January 2025

Accepted for publication 21 February 2025

Published 28 February 2025



CrossMark

Abstract

The Plasma Injector 3 (PI3) experiment at general fusion has been constructed to demonstrate the ability to form plasma targets suitable for compression in a Magnetized Target Fusion machine. To achieve compressive heating to fusion conditions, the target plasmas should have an energy confinement time sufficiently in excess of the compression time. In this work we present a methodology for calculating this timescale and present results for a large set of discharges. Characterization of the plasma current profiles reveals trends and groupings determined by machine settings. The largest energy confinement times have been obtained for discharges with a broad plasma current profile, fresh lithium coating on the device walls, and a near constant toroidal field. We find that PI3 plasmas at 5 ms into the discharge can have thermal confinement times in excess of 10 ms. These meter-scale plasma can thus achieve significant heating if compressed on a timescale of milliseconds.

Keywords: magnetized target fusion, spherical tokamak, experimental plasma physics, plasma confinement, coaxial helicity injection

(Some figures may appear in colour only in the online journal)

1. Introduction

In Magnetized Target Fusion (MTF) a plasma supported by magnetic confinement of thermal energy is compressed in a time shorter than its initial energy confinement time [1, 2], which will result in efficient heating of the plasma to fusion conditions provided that initial temperature is high enough and MHD stability is maintained during compression.

MTF with a liquid metal compression system is an attractive route to commercial energy production because it solves

the first wall problem and minimizes neutron loading to machine structure to acceptable levels [3]. Because it is a pulsed method, only short energy confinement times, on the order of the compression time, are required. It also naturally provides a method of heat extraction via liquid metal circulation and enables tritium breeding using lithium as a reactive component in the liquid metal.

The concept of MTF using an imploding metal liner to heat a magnetized plasma torus to fusion conditions requires a physical separation, or standoff, between the plasma formation system and the compression system. Conventional designs for tokamak formation do not allow for this standoff because the tokamak plasma is entirely enclosed by components that are not able to withstand the operation of the liner compression system.

A formation method that provides physical standoff is Coaxial Helicity Injection (CHI) formation of plasma toroids [4, 5]. This approach naturally provides axial separation

* Author to whom any correspondence should be addressed.



Original Content from this work may be used under the terms of the [Creative Commons Attribution 4.0 licence](https://creativecommons.org/licenses/by/4.0/). Any further distribution of this work must maintain attribution to the author(s) and the title of the work, journal citation and DOI.

by using a coaxial formation system (magnetized Marshall gun [6], or a magnetized coaxial plasma gun) that injects a magnetized plasma ring across a distance into a separate flux conserving compression system.

Transient CHI was initially explored in spheromak research [4] and was developed further for compact spherical tokamaks with the use of a current-carrying central shaft with the HIT [7–9], HIST [10], SPHEX-Rod [11], NU-SpheroTok [12], and TS-2/TS-3 [13] devices. It was then later applied to generate MTF target plasmas at General Fusion with the Plasma Injector 1 [14] and 2 devices (PI1 and PI2), as well as the SPECTOR series of subscale devices [15, 16]. CHI has also been used as a method of plasma formation in conventional tokamaks such as NSTX [17, 18] and QUEST [19]. However, in these devices the subsequent plasma shaping and control is handled by externally controlled magnetic field coils and the plasma is then heated by several auxiliary heating systems.

Previous subscale MTF experiments built around the SPECTOR design, with a lithium coated spherical aluminum flux conserver of inner radius of ≈ 20 cm, compressed compact spherical tokamak plasmas in $160 \mu\text{s}$ using a symmetric detonation of high explosives to implode the aluminum flux conserver. This sequence of experimental devices as part of the Plasma Compression Science (PCS) program at general fusion [20] provided valuable practical guidance and verification of the scalings governing MTF compression, and has been used to inform the design of a next generation of large scale MTF demonstration experiments in which spherical tokamak plasmas will be compressed with electromagnetically compressed solid lithium liners, with a compression time of 2–3 ms.

The Plasma Injector 3 experiment, PI3, has the goal of optimizing the formation of full-scale plasma targets without compressing, in order to demonstrate how to achieve initial conditions that would be suitable for compression to fusion temperatures in the next generation of compression experiments. Motivated by applications to MTF compression experiments, we aim in this work to characterize the instantaneous energy confinement time of a single plasma as implied by diagnostic data in a small window of time around that moment of interest.

The unconventional arrangement needed for plasma formation mechanism standoff in MTF however presents several diagnostic challenges that make it somewhat more involved to determine the energy confinement time in PI3 relative to the methods used in a conventional tokamak as it precludes implementation of a diamagnetic loop diagnostic or total plasma current Rogowski coil. While we are able to accurately measure the plasma current via a set of poloidally distributed magnetic probes at the outer boundary of the plasma, lack of a simple direct measure of plasma loop voltage forces us to make a more complete analysis of the plasma properties and dynamics in order to determine the ohmic heating power, and from that the thermal energy confinement time. Additionally, as the PI3 plasma is not in steady state and has no auxiliary heating, the thermal energy confinement time cannot be determined by the heating power needed to produce a steady state.

Instead, in this work we present a method for determining the required quantities from the other diagnostics and equilibrium reconstruction of the plasma without appeal to a loop voltage. Furthermore, we are able to reveal in detail through these methods the benefits of control of the current driven through the central shaft of PI3, and determine that good plasma performance is enabled by fresh lithium coating on the plasma facing surfaces of PI3.

We proceed to describe the PI3 device and diagnostics systems in section 2. In section 3 we describe the theoretical framework of the energy confinement time. Then, in section 4 we describe the specific methods developed to calculate the required physical quantities from the data provided by the PI3 setup. The results of these calculations are presented in section 5, and in section 6 we discuss further the limitations of the methods as revealed by their application. Finally, conclusions are drawn in section 7.

2. Experimental setup

This section provides a broad overview on the PI3 device (section 2.1) and on the diagnostic suite arranged to monitor PI3 plasmas (section 2.2). Particular emphasis is devoted to the Thomson scattering (TS) system (section 2.3), that measures electron temperature profiles crucial for the calculation of the plasma thermal energy and of the ohmic power. Finally, since our calculation of the energy confinement time relies significantly on reconstructed equilibria, we close the section with a discussion on the equilibrium reconstruction algorithm developed at General Fusion.

2.1. PI3 Device

PI3 first formed spherical tokamak plasmas in November 2017. A major upgrade of the machine followed in 2021, when two Poloidal Field Coils (PFCs) were mounted around the aluminum flux conserver in order to produce the so called buffer flux necessary for a diverted plasma configuration.

A cross section of PI3 is shown in figure 1, while typical values of the main parameters for PI3 plasmas are listed in table 1. The PI3 device is composed of a Marshall gun connected to a spherical aluminum target chamber with a central shaft. Plasma is formed inside the Marshall gun by a ~ 20 kV pulse applied to a deuterium gas cloud with a preexisting poloidal and toroidal field; the resulting $J_r \times B_\phi$ rail-gun force pushes the plasma ring forward dragging with it the embedded magnetic flux. This plasma expands into the target chamber in about $50 \mu\text{s}$, carrying net magnetic helicity, which is the key concept of CHI, and once in the larger volume the plasma undergoes magnetic reconnection and internal reorganization forming a closed magnetic structure that is then trapped in the target chamber and the plasma continues to live for $\sim 20 - 30$ ms. PI3 has a high vacuum system maintained at pressure $p \sim 1 \times 10^{-7}$ Torr. The target chamber and Marshall gun sections of PI3 are periodically coated with lithium using

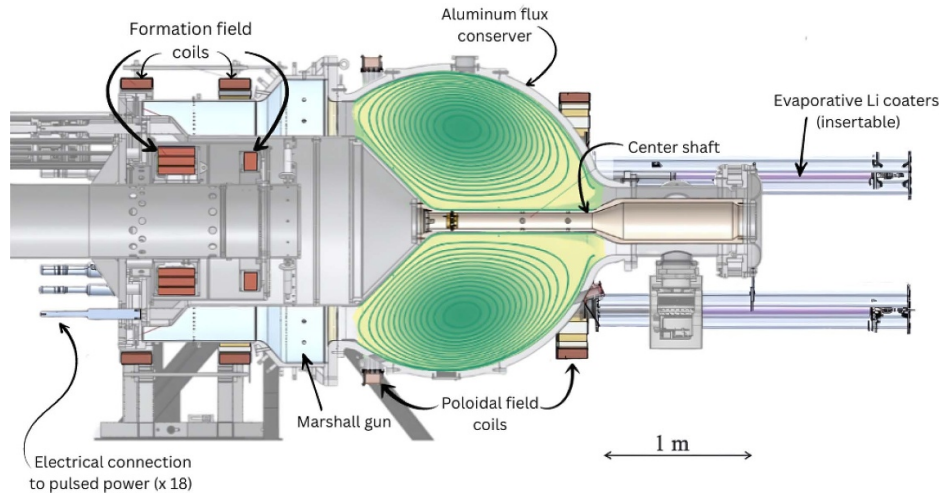


Figure 1. Diagram of the PI3 device.

Table 1. Typical values for main PI3 plasma parameters.

Parameter	Symbol	Value
Vessel inner radius		1 m
Major radius	R_0	0.6 — 0.7 m
Minor radius	a	0.3 — 0.4 m
Elongation	κ	1 — 1.6
Triangularity	δ	-0.15 — +0.1
Poloidal flux	Ψ_{ST}	0.15 — 0.25 Wb
Plasma current	I_{pl}	0.3 — 0.5 MA
Shaft current	I_{sh}	0.8 — 1.2 MA
Electron density	n_e	$2 \times 10^{19} - 6 \times 10^{19} \text{ m}^{-3}$
Temperature	$T_e \sim T_i$	100 — 500 eV
Beta	β	2% — 8%

an evaporative coating method [21]. The target chamber has gate valves for inserting four large lithium coaters during a coating session while the Marshall gun has six smaller coaters.

A pulsed power supply, containing a total of 7.6 MJ divided in two capacitor banks, is employed to drive the so called shaft current, I_{sh} , through the electrical connections along the gun electrodes, the aluminum walls of the flux conserver, and the central shaft. A diagram of the circuit connecting the power supplies to PI3 is plotted in figure 2, where L_{ec} and R_{ec} show the impedance of the electrical connections to PI3 (see figure 1 bottom left) and V_0 is the voltage applied to the machine. The first two-stage bank contains a small power supply ($C_{pf} = 0.2 \text{ mF}$, 35 kV max), termed pre-formation, that initializes breakdown in the Marshall gun, and a large power supply ($C_f = 2.5 \text{ mF}$, 35 kV max), called the formation bank, that delivers the bulk of the energy to the plasma. The second cluster is divided into the so-called peaking bank ($C_{pk} = 27 \text{ mF}$, 10 kV max) and the sustain bank, which sustains the shaft current to less than a 15% drop over 7 ms using 4.8 MJ of stored energy ($C_{st} = 0.2 \text{ mF}$, 10 kV max). The diode in the sustain branch prevents current from flowing backwards into the sustain supply. In this work, the voltage applied to the capacitor banks is also referred to as *setpoint*.

The PI3 magnet system contains a total of six water-cooled electromagnetic field coils. Four coils exist in the plasma injector gun and provide the DC poloidal flux linking the gun electrodes, necessary for plasma formation in CHI. The remaining two coils, located in proximity of the top and of the bottom of the target chamber, create the poloidal magnetic field (i.e. buffer flux) necessary to keep the plasma away from the aluminum wall, and, thus, to produce a diverted plasma configuration. Each coil has an individual power supply comprised of either lead-acid batteries, or supercapacitors, with a shot-variable operating range between 40 and 600 A.

The typical mode of PI3 operation involves the following steps. First, electromagnets are fired to produce the gun flux and the buffer flux in the target chamber. This happens 3 – 4 s before the capacitor banks are fired, in order to allow the vacuum field to soak into the electrodes. Then a ring of 25 piezo-actuated gas puff valves are simultaneously opened for a duration of $\sim 100 - 300 \mu\text{s}$ allowing pressurized deuterium gas to be puffed into the annular gap between the electrodes of the Marshall gun. Once the gas cloud has had enough time to expand and fill this radial distance, the peaking and then pre-formation capacitor banks are fired in the given order and the strong electric field between the electrodes induces plasma

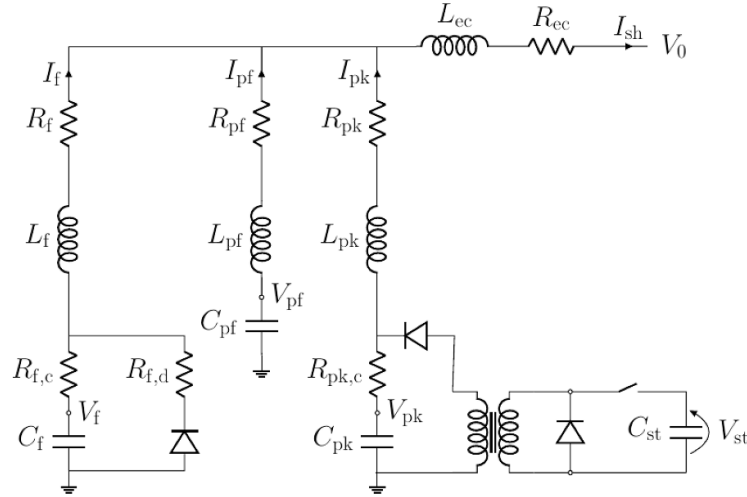


Figure 2. Circuit model for PI3 capacitor bank circuit. Elements L_{ec} and R_{ec} represent the impedance of the electrical connections. Elements C_f , L_f and R_f , together with capacitor module resistance $R_{f,c}$ and diode path resistance $R_{f,d}$, describe the formation bank with current I_f . Elements C_{pf} , L_{pf} and R_{pf} describe the pre-formation bank with current I_{pf} . Elements C_{pk} , L_{pk} and R_{pk} , together with capacitor module resistance $R_{pk,c}$ represent the peaking bank, with current I_{pk} . Capacitor C_{st} represents the sustain capacitor bank, with voltage V_{st} . Voltage V_0 is applied to the machine.

breakdown. As soon as breakdown is detected, the formation capacitor bank is fired driving up to 500 kA of current between the gun electrodes through the plasma, which powers the CHI formation of a spherical tokamak plasma configuration in the target chamber.

Experiments are referred to as *sustained* or *not sustained*, depending on the evolution of shaft current after the plasma is formed. In not-sustained experiments the shaft current drops from $I_{sh} \sim 1$ MA at the beginning of the shot to zero in roughly 30 – 40ms, promoting a fast reduction of the toroidal flux in the flux conserver and inducing a poloidal electric field that drives poloidal current in the plasma. The interaction between the poloidal current and the toroidal magnetic field causes expansion of the plasma volume, compressing the poloidal flux between the LCFS and the walls of the device until force balance is restored. Assuming conservation of the poloidal magnetic flux within the aluminum flux conserver, as the poloidal flux is compressed, toroidal current is driven in the plasma edge, reducing the internal inductance of the toroidal current distribution.

Since the resulting evolution of the safety factor profile, $q(\psi)$, may undermine the stability of the plasma with the occurrence of tearing modes, sawtooth activity or internal reconnection events [22], plasma with improved stability is obtained in sustained experiments, in which the shaft current is sustained ($dI_{sh}/dt \approx 0$) for a few milliseconds using the additional sustain capacitor bank.

2.2. Relevant diagnostic systems

In this work, we adopt a cylindrical coordinate system (R, ϕ, Z) , with Z -axis parallel to the axis of the PI3 central shaft, R the radial distance from the Z -axis, and ϕ the toroidal angle. We use diagnostic data to model the plasma as an axisymmetric equilibrium ($\partial/\partial\phi = 0$), however small

fluctuations away from axisymmetry can also be observed. A summary of relevant diagnostics is given in figure 3.

Surface magnetic field measurements are made with a set of Mirnov coils that are embedded in the shaft and outer vessel of the machine. There are seven unique (R, Z) positions, each with several redundant toroidal locations, with 32 probe locations in total. Each Mirnov probe consists of two B-dot pickup coils sensitive to the toroidal and poloidal magnetic field components. The coils are calibrated [23, 24] in-situ to compensate for the distorting effect of each port well on the magnetic field. Resistive decay of eddy currents flowing around the port well results in a frequency-dependent response curve for the sensor. This response curve is measured during the calibration process by driving a known frequency-swept current pulse through a dedicated calibration coil temporarily mounted inside the PI3 vessel (for the poloidal sensors), or coaxially down through the center shaft and back along the flux conserver (for the toroidal sensors). Then the measured coil signal is compared to a theoretic value of magnetic field strength at the probe location (calculated using a finite element magnetic code [25]) to determine the calibration. The frequency-dependent transfer function response is then calculated for each individual coil by comparing excitation and measured signals and using Wiener deconvolution to extract the underlying response curve. Typically, PI3's Mirnov coils are calibrated up to 35 – 40 kHz (the bandwidth limit of the calibration equipment) with typical residual calibration errors for this measurement of 2%–4% over the frequency range of interest. Frequencies above the calibration range are left uncalibrated and mostly appear as low-amplitude noise superposed to the signal.

During machine operations, the Mirnov coil voltages are measured with a linearized optical isolation circuit which transmits the integrated $B(t) \sim \int V_{coil} dt$ signals as amplitude modulated light transmitted through fiber optics into a Faraday-shielded screenroom that contains optical-input

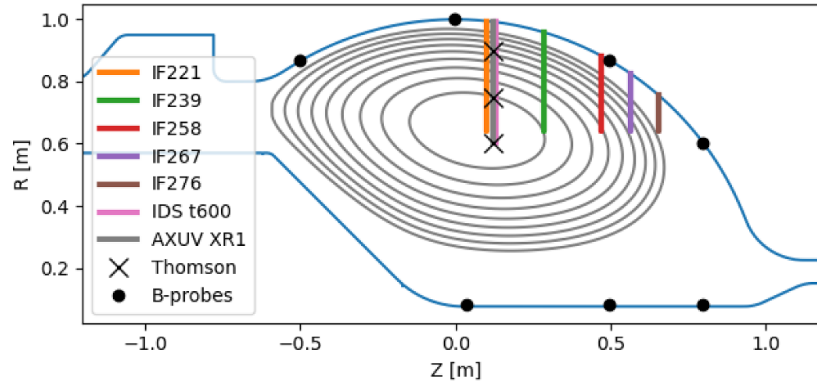


Figure 3. PI3 diagnostic measurement locations projected onto the (R, Z) plane. The diagnostic suite includes five interferometer chords, labeled IF***, the ion Doppler spectroscopy line-of-sight (IDS t600), and the AXUV line-of-sight (AXUV XR1). Thomson Scattering acquisition points and Mirnov probes are shown as black crosses and dots, respectively. Flux contours (gray curves) are shown for a representative Grad–Shafranov equilibrium, omitting open field lines that surround the last closed flux surface. Note that the ion Doppler and AXUV view chords are nearly coincident in (R, Z) .

digitizers. This optical isolation system is highly effective at eliminating the possibility of ground loops and other EM noise contaminating the coil-voltage signals. The optical isolation and integration circuit is calibrated separately by sending a 1 kHz sine-wave pulse through the circuit and fiber optics, thus measuring its scalar transfer factor. This circuit was characterized in bench tests and found to have a flat frequency response up to ~ 200 kHz, well above the calibration range of interest.

Rogowski coils are located on the electrical connections to the pulse power supplies and on the nose of PI3 and monitor the time evolution of the shaft current. Current measurements at the extremes of the machine allow identification of possible arcs in the gun or in the target chamber, potentially detrimental to plasma performance. CHI formation into the flux conserver forbids the use of large internal Rogowski coils for direct measurements of the plasma current. Nonetheless, time-traces of the plasma current can be estimated accurately with a loop integral of poloidal magnetic field at the inner surface of the vessel $I_{pl} = (1/\mu_0) \oint B_{pol}(s) ds$ using the Mirnov probe poloidal measurements as data for a constrained spline interpolation of $B_{pol}(s)$ between measurement points. Calculation of this poloidal loop integral via spline quadrature is independent of plasma profile, and has been verified through comparison to a set of Grad–Shafranov (GS) equilibrium to have a maximum relative error of 8% including measurement error of the probes.

Five interferometer (IF) chords span the edge to the core and measure line-integrated electron density. The IF is a two-color CO_2 -HeNe system [26] where the HeNe is used to subtract out vibration error from the measurement. While the IF vibration subtraction performs well early in a shot, there is increasing vibration error in the density measurement due to a large transverse vibration that becomes significant roughly 8 ms after plasma formation. This is accounted for in the error analysis.

Ion temperature is measured with a narrow fan of four ion Doppler spectroscopy (IDS) co-planar chords with a view of the plasma core, measuring the thermal broadening of the C V 227.089 nm line. The instrumentation for this diagnostic uses a Horiba iHR550 Czerny–Turner spectrometer with a 16-channel linear photomultiplier tube (PMT) array as a detector. Instrumental broadening is subtracted from the measured Gaussian line width in quadrature to determine an average temperature of the carbon ion impurity, which is an emissivity-weighted average temperature along the observation chord. The relative error on T_i due to the quality of the Gaussian fit is typically in the range of 7%–20%. However, due to non-uniformity of plasma properties and carbon abundance the measured value $T_i(t)$ can fluctuate in time by 30% on a timescale of $\sim 10 \mu\text{s}$. Low-pass filtering is applied to the $T_i(t)$ signal before using it as an input to the thermal energy estimate. Carbon impurities are primarily sourced from stainless steel components in the Marshall gun. The thermal equilibration time between the C V impurity population and the deuterium majority species, assessed following [27–29], is found to be smaller than 1 ms in the range of temperature relevant for PI3 plasmas. Carbon impurities are thus expected to be in local thermal equilibrium with the main ion population of the plasma at the reference TS acquisition time, $t_{TS} = 5$ ms. However, the spatial distribution of the C V state is likely to differ from the deuterium ion population because the C V charge state can only exist within a range of electron temperatures that is a subset of what is observed by TS measurement on PI3. In fact, in regions of the plasma where $T_e \gtrsim 300$ eV, carbon predominantly exists in states that are five times or fully ionized [30]. Therefore the IDS measurement of T_i is likely to be insensitive to core ion temperatures.

A multi-filter absolute extreme ultraviolet (AXUV) diodes diagnostic [31] is used to estimate the electron temperature with high time resolution. The AXUV system has a view of

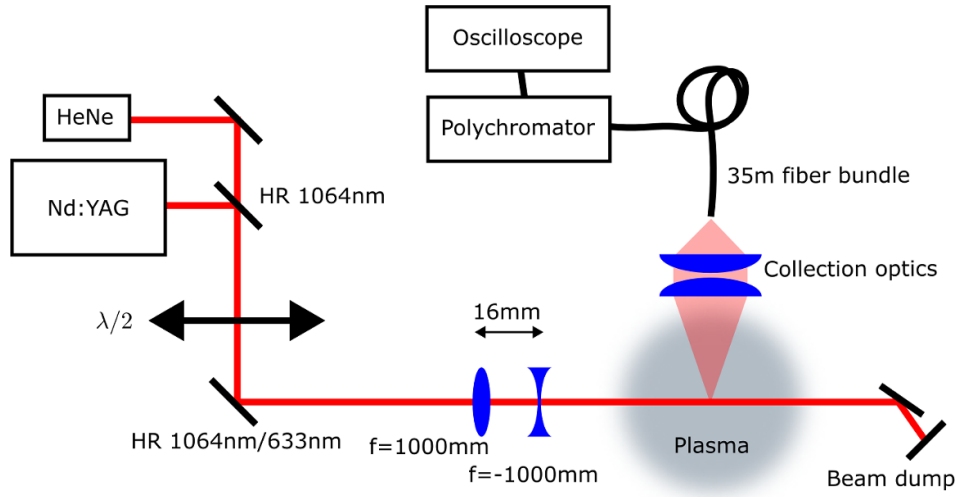


Figure 4. Schematic of the PI3 TS system. Only one of the three collection optic assemblies is shown for clarity.

the plasma core. An extensive overview of the TS system in PI3 is provided in the next section.

2.3. TS system on PI3

2.3.1. Laser and beam delivery. A schematic of the PI3 TS system is shown in figure 4. The system is based on an Innolas SpitLight 2500 Nd:YAG 1064 nm pulsed laser running in single-shot mode, with a pulse duration of around 10 ns and pulse energy of 1.5 – 1.7 J. A 633 nm CW beam from a helium-neon laser is aligned to be co-linear with the 1064 nm beam to facilitate alignment. A half-wave plate is used to control and optimize the polarization angle of the 1064 nm beam. The combined beams are delivered to PI3 via high-reflectivity (HR) mirrors coated for 1064 nm and 633 nm. The beam passes through a half-wave plate to rotate the polarization to optimize the signal amplitude at the detector. The 1064 nm beam travels a path of about 20 m from the laser, after which it has a diameter of about 30 mm, so the beam is gently focused by passing it through two lenses separated by 16 mm. The first lens has a focal length of 1000 mm and the second a focal length of -1000 mm. This combination gives an overall focal length of about 6.5 m, which is approximately the distance from the compound lens to the center of PI3. The laser enters and exits the vacuum via Brewster windows at the end of ~ 2 m steel tubes, each tube with several graphite rings inside forming baffles to reduce stray light. The beam traverses the machine perpendicular to the Z-axis. The beam waist is about 5 mm. After exiting the machine the light is dumped into a pair of absorbing neutral density filter stacks, the first at Brewster's angle to minimize reflection from the front surface.

2.3.2. Collection optics. The laser beam is imaged at three points, corresponding to radii of 600 mm, 747 mm, and 900 mm (shown in figure 3). At each point the scattered light passes through a Kodial glass window and is then collected by a pair of off-the-shelf plano-convex lenses, which combine to form an imaging system with a magnification of about

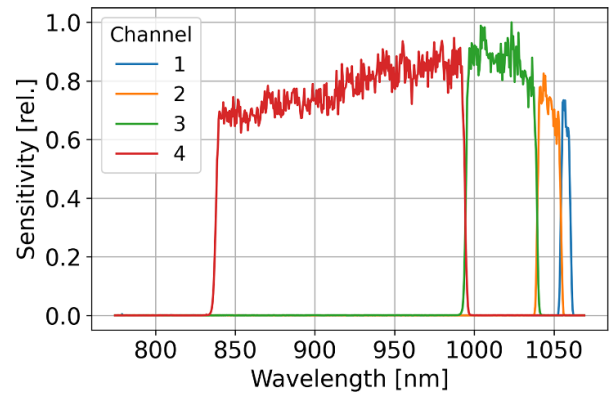


Figure 5. Measured polychromator sensitivity spectrum.

1/3. The lens pairs have diameters of 200 mm, 200 mm, and 100 mm respectively. The f-number at each point is limited by the vacuum window, and is $f/6.12$, $f/5.41$, $f/5.35$ respectively. Each lens pair images the laser beam on to a 35 m-long rectangular multimode fiber bundle. Each fiber bundle has 130 strands, arranged into a rectangle of 3.11 mm by 2.02 mm, meaning a laser beam length of about 9 mm is imaged. Each fiber strand has a core diameter of $210 \mu\text{m}$, a cladding diameter of $230 \mu\text{m}$, and a numerical aperture of 0.285 or f-number of $f/1.68$. The fiber ends are anti-reflection-coated for visible and near-infrared light.

2.3.3. Polychromators and data acquisition. Light from each fiber bundle is directly injected into a UKAEA-manufactured polychromator [32]. The polychromator outputs are AC-coupled to reduce background signal from plasma Bremsstrahlung and line radiation. Data is acquired on oscilloscopes with 8-bit resolution and 1 GS^{-1} sampling rate. Typical polychromator calibration data are shown in figure 5.

2.3.4. Data analysis. Plasma temperatures are extracted via a Bayesian estimation procedure. Firstly, scattered light

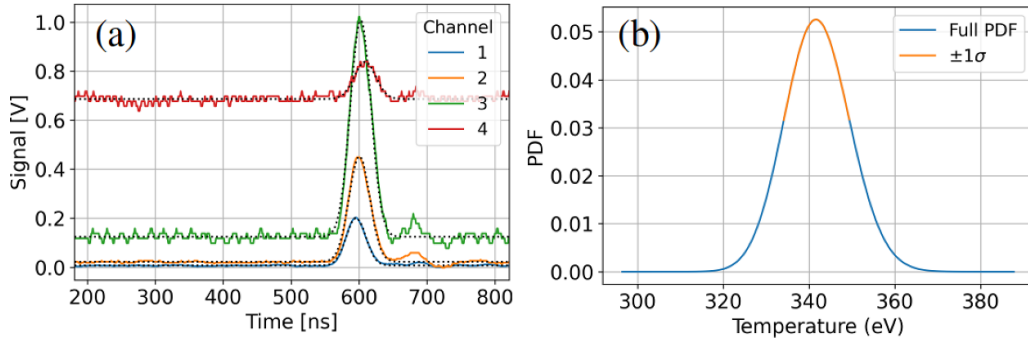


Figure 6. Typical experimental data from the Thomson scattering system for shot number 21 100. (a) Measured Thomson scattering signals. Dotted black lines are Gaussian fits to the data. (b) Probability density function of the plasma having a particular temperature given the data in (a). The yellow curve is centered on the most likely temperature and has a width such that it contains 68.27% of the total area, giving $T_e = 341.6_{-7.5}^{+7.8}$ eV.

amplitudes are measured from polychromator data by fitting Gaussians to measured pulses (see figure 6(a)). These amplitudes are then fed into a Bayesian algorithm [33] which estimates the probability that the data can be explained by the Selden equation [34] assuming a particular plasma temperature (see figure 6(b)). We include uncertainties due to fitting uncertainty, estimated shot noise, and so-called excess noise on the polychromator avalanche photodiodes. This Bayesian analysis is in good agreement with a more naive fitting algorithm when the signal-to-noise ratio (SNR) is high, and provides better quantification of the uncertainty when the SNR is low.

2.4. Equilibrium reconstruction

Physical quantities of interest are estimated from the PI3 diagnostic suite using a Bayesian reconstruction method [35] to estimate the plasma state from a prior distribution over a large 7 or 8 dimensional look-up-table of pre-computed axisymmetric MHD equilibria satisfying the GS equation [36].

The lookup table is constructed to span all plasma states of interest described by the following model. The inputs to the GS solver are the poloidal beta, current profile, pressure profile, and poloidal flux on the boundary. The current and pressure profiles are functions of the normalized poloidal flux which are parameterized using simple functional forms. The boundary condition is a combination of the poloidal flux introduced by the external magnetic coils and the magnetic diffusion into the wall, which is calculated from the field history at the wall surface. Each of these inputs are varied over the range of all plausible values, to create a table with on the order of 1 million GS equilibria, which can also be interpolated. For each equilibrium in the table, synthetic probe values are calculated, as well as physical quantities of interest, such as magnetic energies.

The reconstruction analysis uses Bayes' theorem [37]

$$P(A|B) = \frac{P(B|A)P(A)}{P(B)}, \quad (1)$$

where A represents a given equilibrium from our table, and B represents the measurements taken from the experiment. We

do not assume any prior information, except the assumption that the table spans parameters of interest, postulating that $P(A)$ is a constant, the same for all equilibria. The denominator $P(B)$ is chosen so that $\sum P(A|B) = 1$. Now $P(B|A)$ is the probability of the measurements if equilibrium A were the truth, which is just the aggregate error

$$P(B|A) = \exp\left(-\frac{1}{2} \sum_{\text{probes}} \left(\frac{m'_i - m_i}{\sigma_i}\right)^2\right), \quad (2)$$

where m'_i and m_i are the experimental and synthetic measurements, and σ_i is the measurement uncertainty of each probe. Diagnostic signals are filtered and sampled at prescribed times. In addition, there is a simultaneous solve of the density profile. Synthetic IF and polarimeter measurements are generated using a piece-wise linear density model for each equilibrium. These measurements are included in the $P(B|A)$ calculation above, so that density measurements help to inform the magnetic structure, and magnetic measurements help to inform the density profile.

The output of this process is a posterior probability distribution which varies smoothly over the (interpolated) table of GS equilibria. From this, we can derive probability density functions for any parameter of interest. This is how error bars are derived for all quantities. These include poloidal magnetic energy, q -profile, beta, etc.

Because the density profile has uncertainty for each equilibrium (unlike magnetic quantities), some special treatment is required to derive uncertainties for density-dependent quantities. Using the piecewise linear density model, the synthetic density measurements for each equilibrium are linear functions of the density model parameters w , a vector. We can then represent this linear relationship with a matrix M , and substitute Mw for the synthetic measurements in equation (2) to find a normal posterior distribution over the density model parameters for each equilibrium:

$$P(w|m) = \exp\left(-\frac{1}{2} (Mw - m)^T C_m^{-1} (Mw - m)\right) \quad (3)$$

where C_m is the covariance matrix of the measurement noise, which is diagonal in our case. This is a normal distribution \mathcal{N} over w , given in terms of m , M and C_m by

$$w = \mathcal{N} \left((M^T C_m M)^{-1} (M^T C_m^{-1}) m, (M^T C_m M)^{-1} \right) \quad (4)$$

where the arguments of \mathcal{N} are the mean and variance. The total posterior distribution over the density parameters for the table of all equilibria is therefore a weighted sum of these normal distributions, also called a Gaussian mixture model, from which we extract statistics for each point in the density profile. In the case of the particle inventory uncertainty, the distribution per-equilibrium is calculated, and statistics are then tabulated from the resulting mixture model.

Statistical moments of the physical properties of the set of best-matching equilibria are then used as the primary inputs for the calculation of the thermal energy confinement time and its error.

3. Calculation of the thermal energy confinement time

For each PI3 plasma, equilibrium reconstruction provides the maximum and the minimum radial distance from the Z-axis for 21 magnetic flux surfaces enclosing a normalized poloidal flux $\bar{\psi}_k = 0.05 k$ with $k = 0, 1, 2, \dots, 20$. Here, $k = 0$ and $k = 20$ correspond to the magnetic axis and to the last closed flux surface (LCFS), respectively. It is, then, immediate to compute the minor radius of each magnetic flux surface as

$$r(\bar{\psi}_k) = \frac{R_{\max}(\bar{\psi}_k) - R_{\min}(\bar{\psi}_k)}{2}, \quad (5)$$

where $R_{\max}(\bar{\psi}_k)$ and $R_{\min}(\bar{\psi}_k)$ are the maximum and the minimum radius of the flux surface $\bar{\psi}_k$, respectively. In the following, we will adopt the normalized minor radius, defined as $\rho(\bar{\psi}_k) = r(\bar{\psi}_k)/a$ with a minor radius of the LCFS, as coordinate for the magnetic flux surfaces.

The total plasma thermal energy is the sum of contributions from the electron population and from all ion populations in the plasma [38, 39]

$$\begin{aligned} E_{\text{th}}(t) &= E_{\text{th,e}}(t) + \sum_s E_{\text{th,s}}(t) \\ &= \frac{3}{2} \int_0^1 n_e(\rho, t) \left[T_e(\rho, t) + \frac{T_i(\rho, t)}{Z_{\text{ave}}} \right] \frac{\partial V}{\partial \rho} d\rho, \quad (6) \end{aligned}$$

where $n_e(\rho, t)$ and $T_e(\rho, t)$ are the flux surface average electron number density and temperature, respectively. In order to account for impurities in the plasma, we assume isothermal ion species, i.e. $T_s(\rho, t) = T_i(\rho, t) \forall s$, and introduce the average ion charge, defined as $Z_{\text{ave}} \equiv n_e(\rho, t) / (\sum_s n_s(\rho, t))$, in order to cast the ion contribution in terms of the electron density. Since the level and the evolution of the impurity populations are not properly characterized in PI3, we assume Z_{ave} , as well as Z_{eff} introduced later, uniform in the plasma and constant in time. In particular, the results presented in this manuscript are obtained for $Z_{\text{ave}} = 1.5 \pm 0.5$ and $Z_{\text{eff}} = 2 \pm 1$.

The only source of heating for PI3 plasmas is ohmic power:

$$P_{\Omega}(t) = \int_0^1 \eta(\rho, t) [J(\rho, t)]^2 \frac{\partial V}{\partial \rho} d\rho, \quad (7)$$

where $J(\rho, t)$ is the plasma current density and $\eta(\rho, t)$ is the plasma resistivity. Following Wesson [27] we use

$$\eta(\rho, t) = \gamma_{\text{neo}}(\rho, t) f_i(Z_{\text{eff}}) \eta_S(\rho, t). \quad (8)$$

The Spitzer resistivity in units [$\Omega \text{ m}$] is given as

$$\eta_S(\rho, t) = 5.26 \times 10^{-5} \frac{\ln \Lambda(\rho, t)}{(T_e(\rho, t))^{3/2}}, \quad (9)$$

with $\ln \Lambda(\rho, t) = 31.3 - 0.5 \ln n_e(\rho, t) + \ln T_e(\rho, t)$ the Coulomb logarithm, T_e in eV, and n_e in m^{-3} . The factor $f_i(Z_{\text{eff}})$ is a correction to take into account the increase in resistivity due to impurities, where the effective ion charge is defined as $Z_{\text{eff}} \equiv \sum_s Z_s^2 n_s(\rho, t) / n_e(\rho, t)$, with Z_s charge of the s th ion species. It is given by $f_i(Z) = Z[1 + 0.27(Z - 1)] / [1 + 0.47(Z - 1)]$. The neoclassical correction, $\gamma_{\text{neo}}(\rho, t)$, is given by

$$\gamma_{\text{neo}}(\rho, t) = \frac{1}{(1 - f_T^*(\rho, t))(1 - C f_T^*(\rho, t))}, \quad (10)$$

with $f_T^*(\rho, t) = f_T / [1 + (0.58 + 0.20 Z_{\text{eff}}) \nu_{*e}]$ the fraction of trapped electrons f_T corrected by the dimensionless collisionality ν_{*e} related to banana orbits and $C = (0.56 / Z_{\text{eff}})(3 - Z_{\text{eff}}) / (3 + Z_{\text{eff}})$. Also from Wesson [27], $\nu_{*e} = \varepsilon^{-3/2} R q / (v_{Te} \tau_e)$ with ε , R and q the inverse aspect ratio, major radius and safety factor of the flux surface, $v_{Te} = (T_e / m_e)^{1/2}$ the electron thermal speed and $\tau_e = 3(2\pi)^{3/2} \varepsilon_0^2 m_e^{1/2} T_e^{3/2} / (n_e e^4 \ln \Lambda)$ the electron collision time. The collisionless-plasma trapped fraction is calculated using

$$f_T = 1 - \frac{(1 - \varepsilon)^2}{(1 - \varepsilon^2)^{1/2} (1 + 1.46 \varepsilon^{1/2})}. \quad (11)$$

Another neoclassical effect that must be included in a complete analysis of the power balance in the plasma is the bootstrap current [40]. This effect contributes to reduce the resistive plasma current and, hence, unlike the corrections described earlier, the total ohmic dissipation. Profiles of the bootstrap current in PI3 plasma were obtained following the works presented in [27, 40, 41] and produce a total reduction of $P_{\Omega}(t)$ typically below 10%, for the dataset used in section 5.2. In the model presented in this manuscript, we, then, neglect the effect of the bootstrap current, and postpone a complete treatment on the topic to future works.

For ohmically heated plasmas, the time evolution of the plasma thermal energy can be described by the following energy balance equation [4, 27]

$$\frac{dE_{\text{th}}}{dt}(t) = -\frac{E_{\text{th}}(t)}{\tau_E(t)} + P_{\Omega}(t), \quad (12)$$

where the first term on the RHS accounts for all heat loss mechanisms (diffusion, turbulent transport processes, radiated power) and it is cast in terms of the thermal energy confinement time, $\tau_E(t)$, which can, then, be written as

$$\tau_E(t) = \frac{E_{\text{th}}(t)}{P_{\Omega}(t) - dE_{\text{th}}/dt}. \quad (13)$$

This is the core equation of the work, routinely used for the calculation of the energy confinement time in PI3 plasmas. In the following section, we will dive into the details of the calculation and present models and assumptions adopted to compute τ_E from equation (13).

4. Methods

In this section, we present the assumptions and the techniques adopted in this work to compute the plasma thermal energy, $E_{\text{th}}(t)$, the time derivative of the thermal energy dE_{th}/dt , and the ohmic power, $P_{\Omega}(t)$. The calculation of the thermal energy confinement time, $\tau_E(t)$, is then straightforward using equation (13). The notation adopted in the rest of the manuscript is presented in table 2.

4.1. Calculation of the thermal energy

The calculation of the plasma thermal energy using equation (6) relies on profiles of the flux surface average electron density, $n_e(\rho, t)$, electron temperature, $T_e(\rho, t)$, and ion temperature, $T_i(\rho, t)$. Here, such profiles are obtained by fitting measured or reconstructed profiles to the form

$$f(\rho, t) = f_0(t) (1 - \rho^2)^{\alpha(t)}. \quad (14)$$

The two parameters are $f_0(t)$, the value of the profile on the magnetic axis, and $\alpha(t)$, the exponent determining the shape of the profile. The `scipy` function `curve_fit` [42] is used to obtain the best fit values $f_0(t)$ and $\alpha(t)$, and the corresponding covariance matrix. The error on the profile in equation (14) is assessed combining the original error (from measurements or equilibrium reconstruction) with a fit error computed as

$$\Delta f(\rho, t) = f(\rho, t) \left[\frac{c_{00}}{(f_0(t))^2} + c_{11} [\log(1 - \rho^2)]^2 + \frac{2c_{10}}{f_0(t)} \log(1 - \rho^2) \right]^{1/2}, \quad (15)$$

with c_{lm} an element of the covariance matrix.

The flux surface average electron temperature profile, $T_e(\rho, t)$, is obtained fitting the three TS points, as shown in figure 7(a). Here, the red dots and the blue profile show TS T_e measurements and the best fit for PI3 shot 21 100 at $t_{\text{TS}} = 5$ ms, respectively. The magnetic flux surface of the outermost TS point ($R = 900$ mm) varies in the range $\bar{\psi} \approx 0.6 - 0.7$ (corresponding to $\rho \approx 0.6 - 0.75$) according to the plasma elongation and volume. Outside of this surface, equation (14) assumes a monotonic drop of $T_e(\rho, t)$, forcing the profile to go to zero or

Table 2. Notation adopted in the manuscript. The quantity g is an arbitrary function.

Operation	Notation
IF line integrated measurement	$\bar{n}_e(t)$
AXUV chord measurement	$\bar{T}_e(t)$
volume average	$\langle g \rangle(t)$
flux surface average profile	$g(\rho, t)$

to an arbitrary low value at the plasma edge. Because our current diagnostic suite cannot inform a realistic T_e in proximity of the LCFS, we currently exclude from our analysis contributions produced outside $\bar{\psi} = 0.9$.

The volume average electron temperature is computed as

$$\langle T_e \rangle(t) = \int_0^1 T_e(\rho, t) \frac{\partial V}{\partial \rho} d\rho / \int_0^1 \frac{\partial V}{\partial \rho} d\rho, \quad (16)$$

and it is found to be $\langle T_e \rangle(t_{\text{TS}}) \approx 190$ eV for shot 21 100 in figure 7(a).

The calculation of dE_{th}/dt requires time resolution in the T_e measurement, clearly not provided by the single TS acquisition. To compensate for this limitation, the time evolution of the electron temperature is obtained combining the TS data at time t_{TS} with the AXUV $\bar{T}_e(t)$. In particular, it is produced normalizing the AXUV $\bar{T}_e(t)$ to the core TS T_e ($R = 600$ mm) at t_{TS} , in a way similar to what shown in [43–45], and using the values of AXUV $\bar{T}_e(t)$ as core T_e at $t_- = t_{\text{TS}} - 1$ ms and $t_+ = t_{\text{TS}} + 1$ ms. Assuming constant α_{T_e} in the time interval from t_- to t_+ , we can then build T_e profiles of the form $f(\rho, t) = f_0(t) (1 - \rho^2)^{\alpha_{T_e}}$ at $t = t_-, t_+$. As explained in [43–45], comparing T_e from soft x-rays filtered signals and TS core T_e measurements is reasonable in plasmas with peaked T_e and n_e profiles, due to bremsstrahlung emission being proportional to $n_e^2 T_e^{1/2}$. For PI3 shots performed with the sustain capacitor bank, as those considered in the manuscript, both electron temperature and electron density profiles peak in the plasma core. This region may then be considered the dominant source of soft x-rays in the plasma.

An example of the results produced by this approach is given in figure 7(b) for shot 21 100. Here, the three TS measurements at $t_{\text{TS}} = 5$ ms are plotted together with the blue AXUV $\bar{T}_e(t)$. The resulting time-traces of the core electron temperature and of $\langle T_e \rangle$ from t_- to t_+ are shown as black squares and dots, respectively. In shots without AXUV measurements, the $T_e(\rho, t)$ fit profile is assumed constant in the 2 ms-long interval around t_{TS} , unless other measurements (IF \bar{n}_e or plasma current) show evidence of crashes in the time interval of interest. In this case, the shot is discarded.

Flux surface average electron density profiles are provided by equilibrium reconstruction. However, for this analysis the fit operation using equation (14) is applied as well, because it provides a standard analytical expression for the profile and allows to quantify the deviation of the reconstructed profile from the analytical model. Error bars on the electron density fit, $n_e(\rho, t)$, are computed from the combination of three contributions: the error of the reconstructed profile, the fit error

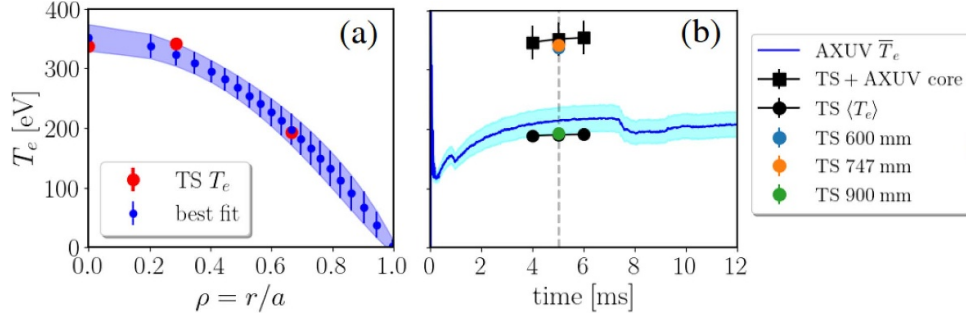


Figure 7. (a) TS T_e measurements for PI3 shot 21 100 at $t_{TS} = 5$ ms (red dots) and corresponding best fit (blue). (b) AXUV \bar{T}_e time-trace (blue) with TS measurements at $t_{TS} = 5$ ms (shown by dashed gray line). The final core T_e and volume average $\langle T_e \rangle$ are shown as black squares and dots, respectively.

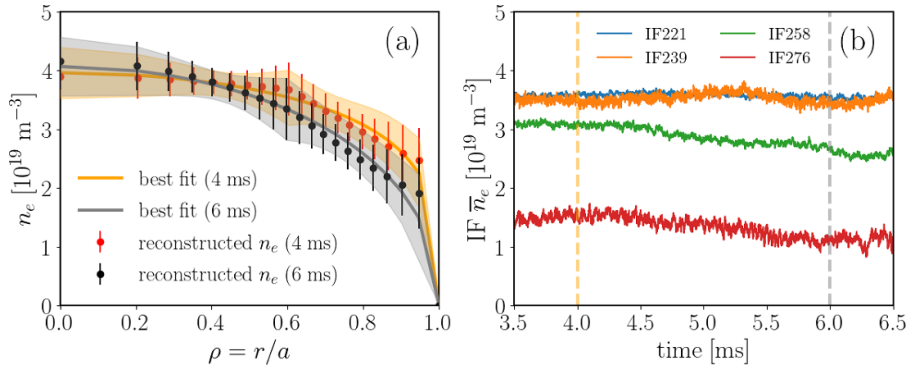


Figure 8. (a) Profiles of reconstructed electron density and corresponding best fit at time t_- and t_+ for shot 21 100 with $t_{TS} = 5$ ms. (b) Time-traces of average electron density measured along the interferometer chords available during shot 21 100. Dashed vertical lines show (orange) t_- and (gray) t_+ . The trajectories of the IF chords are shown in figure 3. Note that each IF measurement is divided by the length of the corresponding chord, and thus has units m^{-3} .

from equation (15), and the squared distance of each point in the reconstructed profile from the corresponding point in the fit. Examples of reconstructed profiles and related fits are plotted in figure 8(a) for shot 21 100 at time t_- and t_+ . The trend of the two density profiles can be validated against the average electron density, $\bar{n}_e(t)$, measured along the IF chords available in this shot, shown in figure 8(b). For example, the mild reduction in $\bar{n}_e(t)$ measured by the edge-most IF chords, i.e. IF258 and IF276, is mirrored by the drop of the gray profile in figure 8(a) for $\rho > 0.6$. The volume average electron density is computed with the same operation introduced in equation (16), which yields $\langle n_e \rangle(t_{TS}) \approx 2.83 \times 10^{19} \text{ m}^{-3}$ for shot 21 100.

The last quantity necessary in the calculation of the plasma thermal energy is the flux surface average ion temperature, $T_i(\rho, t)$. We model this profile assuming $\alpha_{T_i} = \alpha_{T_e}$, i.e. the same shape for the electron and ion temperature profiles, and using IDS measurements as core value for the profile, $f_0(t)$. More specifically, we assess the parameter $f_0(t)$ in equation (14) as the mean T_i from the four measurements from the IDS fan, which is too narrow to provide space resolution for T_i . Figure 9 shows IDS measurements in the first 10 ms of shot 21 100, where the blue curve is the time-trace of the mean IDS T_i while the values and errors used in the profile $T_i(\rho, t)$ are shown in magenta. The four transparent curves in the background show the actual IDS measurements. After the

initial drop in T_i , the error on the measurement along each IDS chord grows from $\sim 10\%$ to $\sim 40\%$ during the interval shown in figure 9 (not reported for matters of clarity).

For the calculation of the error on $T_i(\rho, t)$, we adopt equation (15) and remove the term containing the off-diagonal element, which always reduces the total error, being $c_{10} > 0$. We get

$$\Delta T_i = T_i(\rho, t) \left[\left(\frac{\Delta T_i(0, t)}{T_i(0, t)} \right)^2 + \left[\Delta \alpha_{T_i}(t) \log(1 - \rho^2) \right]^2 \right]^{1/2}, \quad (17)$$

where $\Delta T_i(0, t)$ and $\Delta \alpha_{T_i}(t)$ are the error on the mean T_i (magenta in figure 9) and the fit error on α_{T_e} , respectively. The artificial increase of the T_i error bars is meant to balance the lack of experimental evidence for the choice of equation (14) to model $T_i(\rho, t)$.

Finally, the plasma thermal energy, E_{th} , is assessed using equation (6) with average ion charge, $Z_{ave} = 1.5 \pm 0.5$, and flux surface volume provided by the equilibrium reconstruction. Error bars on the thermal energy are computed with a Monte Carlo (MC) approach. In the MC algorithm, we create $N_{MC} = 10^4$ iterations of each profile ($n_e(\rho, t)$, $T_e(\rho, t)$, and $T_i(\rho, t)$) and for Z_{ave} and compute E_{th} from equation (6) for each iteration. Since the resulting population of E_{th} samples

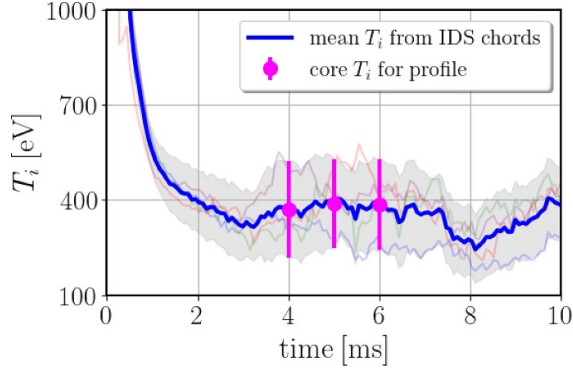


Figure 9. (Blue) Time-trace of the mean IDS T_i for PI3 shot 21 100 obtained from measurements along the four IDS chords (shown transparent in the background). Mean T_i and error bars used to build the profile in equation (14) at time t_- , t_{TS} , t_+ are shown in magenta.

displays a slight positive skewness, we use the 50th percentile, $E_{th,50}$, of the distribution as median, and pick the 10th, $E_{th,10}$, and the 90th percentiles, $E_{th,90}$, to assess the deviation from the median. In particular, the error on E_{th} is defined as the mean between $|E_{th,50} - E_{th,10}|$ and $|E_{th,50} - E_{th,90}|$. The choice of the 10th and 90th percentiles over the 16th and 84th, corresponding to the Gaussian standard deviation, is meant to yield a more accurate estimate of the error for a skewed distribution.

A linear fit of the thermal energy around the TS acquisition time (from t_- to t_+) is performed and the resulting slope (with corresponding error from the covariance matrix returned by `curve_fit`) is used as time-derivative of the thermal energy, dE_{th}/dt .

4.2. Calculation of the ohmic power

In this section, we describe a method for the calculation of the ohmic power, $P_{\Omega}(t)$, in PI3 plasmas, based on profiles of the flux surface average toroidal current density, $J_{\phi}(\rho, t)$, and of the plasma resistivity, $\eta(\rho, t)$.

In general, assessing the total ohmic power requires to take into account contributions from $J_{\phi}(\rho, t)$ and from the poloidal plasma current density, $J_{pol}(\rho, t)$. Nonetheless, a preliminary analysis based on the total toroidal plasma current, the total poloidal plasma current, and on the toroidal magnetic flux produced by the poloidal plasma current suggests that the contribution of $J_{pol}(\rho, t)$ to the total ohmic power never exceeds 10%, and can, thus, be neglected in this first iteration of the method, for simplicity.

Since the toroidal current density is not a flux surface function, GS equilibria in the reconstruction table do not provide 1D profiles of $J_{\phi}(\rho, t)$ by default. Nonetheless, each equilibrium contains information on the geometry of the magnetic flux surfaces and on the total toroidal current flowing within each magnetic flux surface with $\bar{\psi}_k = 0.05 k$ for $k = 1, 2, \dots, 20$, here called $I_{tor}(\rho_k, t)$, where ρ_k is the normalized radius of the k th magnetic flux surface. It is, thus, possible to

define a flux surface average toroidal current density as

$$J_{\phi}(\rho_k, t) = \frac{I_{tor}(\rho_k, t) - I_{tor}(\rho_{k-1}, t)}{A_{pol}(\rho_k, t) - A_{pol}(\rho_{k-1}, t)}, \quad (18)$$

where the numerator and the denominator on the RHS are the toroidal current flowing between the k th and on the $(k-1)$ th flux surface, and the area of the poloidal ring between the k th and the $(k-1)$ th flux surfaces, respectively. Current density profiles are computed using equation (18) in all equilibria contained within the 4σ ensemble created by the Bayesian fit on the reconstruction table. From the resulting population of profiles, we extract the mean and the standard deviation to obtain $J_{\phi}(\rho, t)$ similar to what shown in figure 10(a) for shot 21 100. Error bars decrease near the plasma edge, where magnetic measurements from the Mirnov probes allow to constrain equilibrium reconstruction with less uncertainty.

A validation of the toroidal current density profiles comes from the comparison of the current computed as $I_j(t) = \int_{A_{pol}} J_{\phi}(A_{pol}, t) dA_{pol}$ with the results of a spline calculation from the Mirnov probe signals, $I_{sp}(t)$, shown in figure 10(b). Here, it is possible to see that $I_j(t)$ (blue stars) exceeds $I_{sp}(t)$ (green) by 5%–10%. In order to eliminate the offset in $I_j(t)$, we multiply the $J_{\phi}(\rho, t)$ profiles by the scaling factor computed as $w(t) = I_{sp}(t)/I_j(t)$.

Beside the current density, resistivity is a crucial ingredient in the calculation of P_{Ω} . Profiles of the Spitzer resistivity, the neoclassical correction, and the total plasma resistivity are obtained using (9), (10), and (8), respectively. The resulting profiles are shown in figure 11 for shot 21 100 at $t_{TS} = 5$ ms. The top panel contains profiles of the input quantities to the γ_{neo} calculation, i.e. electron temperature (blue), $T_e(\rho, t_{TS})$, electron density (red), $n_e(\rho, t_{TS})$, and the safety factor (yellow), $q(\rho, t_{TS})$. The central panel shows the inverse aspect ratio of the magnetic flux surfaces (gray), $\varepsilon(\rho, t_{TS}) = r(\rho, t_{TS})/R_0(\rho, t_{TS})$, which grows from $\varepsilon = 0$ up to ≈ 0.8 at the plasma edge, the fraction of trapped electrons, $f_T = f_T(\varepsilon)$, and $f_T^*(\rho, t_{TS})$, which takes into account the collisionality due to banana orbits. Finally, the bottom panel displays the results of the calculation: Spitzer resistivity (blue), neoclassical correction (green), γ_{neo} , and total plasma resistivity (orange) for $Z_{eff} = 2 \pm 1$.

Combining the toroidal current density and the resistivity profiles, we compute ohmic heating density profiles, $p_{\Omega}(\rho, t) = \eta(\rho, t) [J_{\phi}(\rho, t)]^2$ and, from this, the total ohmic power in the plasma at the TS acquisition time

$$P_{\Omega}(t_{TS}) = \int_0^{\bar{\psi}=0.9} p_{\Omega}(\rho, t_{TS}) \frac{\partial V}{\partial \rho} d\rho, \quad (19)$$

where the integral extends to the magnetic flux surface with normalized poloidal flux $\bar{\psi} = 0.9$. The profile of $p_{\Omega}(\rho, t_{TS})$ for shot 21 100 at the TS acquisition time is shown with a dashed blue curve in figure 12(a) together with the corresponding profiles of (red) $J_{\phi}(\rho, t)$ and (green) $\eta(\rho, t)$. The current profile in this shot produces a hollow ohmic heating density peaked at $\rho \sim 0.6$ ($\bar{\psi} \sim 0.5$). Error bars on $p_{\Omega}(\rho, t)$ and

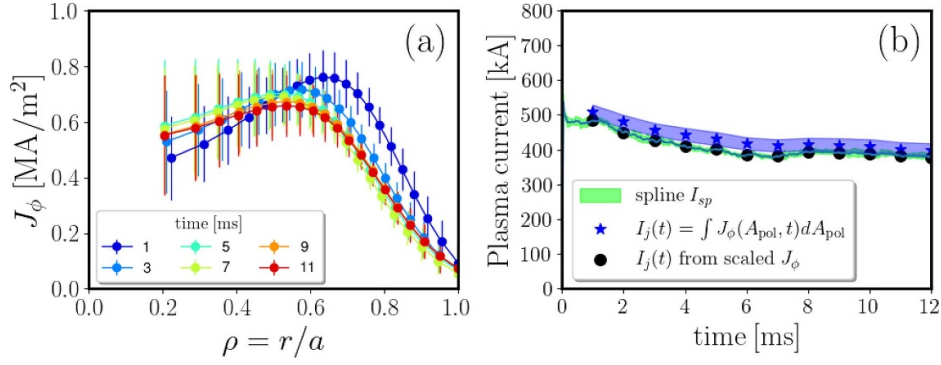


Figure 10. (a) Time evolution of the flux surface average toroidal current density profiles, $J_\phi(\rho, t)$, in shot 21 100. Note that $J_\phi(\rho, t)$ is not defined for $\rho \lesssim 0.2 \approx \rho(\bar{\psi} = 0.05)$ because $\bar{\psi} = 0.05$ is the innermost flux surface on which I_{tor} is given. For this flux surface we compute $J_\phi(\rho \approx 0.2, t) = I_{\text{tor}}(\rho \approx 0.2)/A_{\text{pol}}(\rho \approx 0.2)$. The profiles in this panel are already scaled by the multiplicative factor obtained from the ratio of the total toroidal currents. (b) Total toroidal plasma current produced by the spline calculation of the magnetic signals (green) and integral of the original $J_\phi(\rho, t)$, i.e. $I_j(t)$ (blue stars). The total plasma current computed from the scaled $J_\phi(\rho, t)$ is shown as black dots.

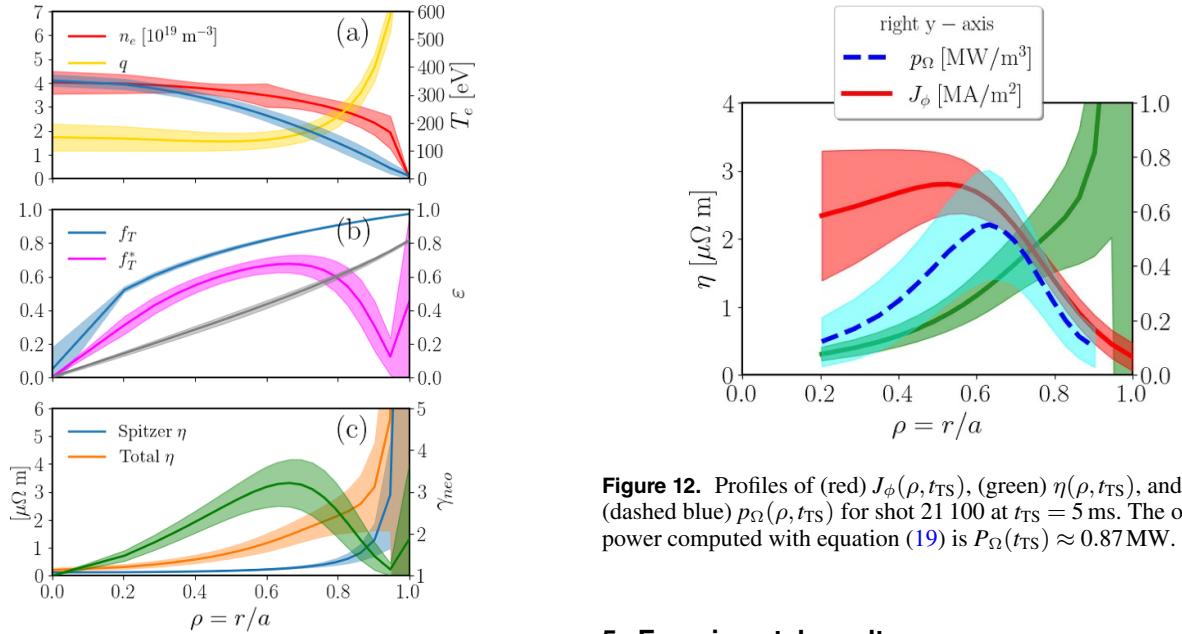


Figure 11. Profiles involved in the calculation of the neo-classical correction to the Spitzer resistivity, $\gamma_{\text{neo}}(\rho, t_{\text{TS}})$, for shot 21 100, at the TS acquisition time, $t_{\text{TS}} = 5$ ms, assuming $Z_{\text{eff}} = 2 \pm 1$. Legends in each panel refer to the leftmost y-axis. (a) Electron temperature fit from TS measurement (blue), electron density fit from reconstructed profile (red), and safety factor q (yellow). (b) Inverse aspect ratio ε (gray), fraction of trapped electrons in the case of zero collisionality related to banana orbits (blue), and f_T^* (magenta), from equation (10). (c) Neoclassical correction (green), Spitzer (blue) and total (orange) resistivity.

on $P_\Omega(t)$ are computed using a MC algorithm analogous to what described earlier, with $N_{\text{MC}} = 10^4$ iterations of $\eta(\rho, t)$, $J_\phi(\rho, t)$. The integral in equation (19) is then computed N_{MC} times, and, since the resulting distribution is roughly Gaussian, we pick the 50th percentiles as the median and the mean distance of the median from the 16th, and the 84th percentiles as standard deviation.

Finally, the energy confinement time, τ_E , is computed from equation (13), with the same MC approach.

Figure 12. Profiles of (red) $J_\phi(\rho, t_{\text{TS}})$, (green) $\eta(\rho, t_{\text{TS}})$, and (dashed blue) $p_\Omega(\rho, t_{\text{TS}})$ for shot 21 100 at $t_{\text{TS}} = 5$ ms. The ohmic power computed with equation (19) is $P_\Omega(t_{\text{TS}}) \approx 0.87$ MW.

5. Experimental results

PI3 control parameters define a large operative space containing plasmas with different properties and quality of energy confinement. In section 5.1, we present an approach to classify PI3 experiments based on plasma internal inductance and toroidal magnetic flux. We describe and compare three main classes of experiments and observe that larger energy confinement times are obtained for plasmas with broad current density profile, where plasma thermal energy can go up to $E_{\text{th}} \approx 8 - 9$ kJ and the current profile is less prone to disruptive instabilities. For this category of shots, we then present the variation of $\langle T_e \rangle$ and of τ_E with the number of shots since the last lithium coating (section 5.2).

5.1. Time evolution of the current and of the ohmic heating density profiles for different formation and sustain setpoints

Knowledge of the toroidal current profile in ohmically heated plasmas is crucial to develop a solid understanding of the

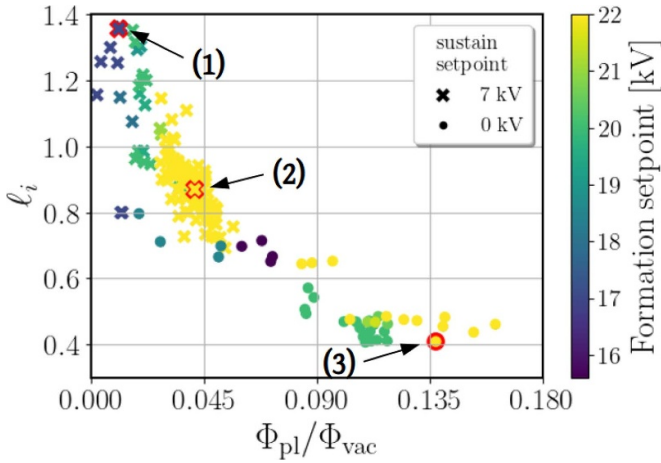


Figure 13. Map of internal inductance, ℓ_i , as a function of the normalized toroidal flux, $\Phi_{\text{pl}}/\Phi_{\text{vac}}$, for shots performed (crosses) with and (dots) without sustain. The color scheme shows the setpoint of the formation capacitor bank. All quantities in the map are taken at $t = 5$ ms. Instances labeled 1, 2, and 3 (shots 21 284, 21 119, 22 289 respectively) are examples of shots with high, intermediate, and low ℓ_i , respectively.

power balance in the plasma and of the plasma MHD stability. A first classification of the toroidal current distribution in the plasma can be done with the internal inductance defined as $\ell_i = \langle B_{\text{pol}}^2 \rangle / \langle B_{\text{pol}} \rangle_L^2$ where $\langle B_{\text{pol}}^2 \rangle$ is the volume average of B_{pol}^2 inside the LCFS and $\langle B_{\text{pol}} \rangle_L = \oint B_{\text{pol}} dl / \oint dl$ is the line average of B_{pol} along the LCFS flux contour in the poloidal plane. The internal inductance is low, $\ell_i \sim 0.4$, for hollow current profiles and grows up to $\ell_i \sim 1.5$ as the current distribution becomes more peaked. Figure 13 shows a map of ℓ_i as a function of a dimensionless toroidal flux defined as the ratio of the toroidal flux produced by poloidal plasma current, Φ_{pl} , and the vacuum toroidal flux from the shaft current, Φ_{vac} . The figure contains data at $t = 5$ ms for a set of 157 shots performed with fresh lithium coating (shots since last lithium coating ≤ 30). In general, the vacuum toroidal flux is one or two orders of magnitude larger than the plasma contribution, mostly depending on the decay rate of the shaft current. The vacuum toroidal flux drops faster in time when the shaft current is not sustained. In these cases, a strong poloidal current induces high Φ_{pl} . Conversely, for shots with sustained shaft current, Φ_{vac} decays at a slower rate, inducing very little poloidal current in the plasma. Figure 13 shows that ℓ_i at $t = 5$ ms decreases exponentially as we increase the normalized toroidal flux from $\Phi_{\text{pl}}/\Phi_{\text{vac}} \sim 0$ to roughly 0.18.

We can observe that sustaining the shaft current seems to be crucial in order to produce plasmas with internal inductance $\ell_i > 0.8$ at $t = 5$ ms, whereas only not sustained shots are found for $\ell_i \lesssim 0.65$. In the area in between these boundaries, there is a narrow region accessible with and without sustain. Additionally, we note that, for both groups of experiments, the internal inductance drops as we raise the voltage of the formation capacitor bank. In order to analyze more comprehensively

the differences between plasmas in figure 13, we compare in figure 14 profiles of $J_{\phi}(\rho, t)$ and $q(\rho, t)$ for instances labeled 1, 2, and 3 in the time interval $t = 1 - 10$ ms. PI3 control parameters for these three cases, corresponding to shot number 21 284, 21 119, and 22 289, are listed in table 3. Toroidal plasma current profiles are plotted in the leftmost column of figure 14. As the internal inductance is reduced, moving from point 1 down to point 3 in figure 13, $J_{\phi}(\rho, t)$ evolves from a profile peaked in the magnetic axis (figure 14(1a)), to a broad profile, with a more uniform current distribution in the plasma (figure 14(2a)), to, eventually, a very hollow profile, with most of the toroidal current flowing at the plasma edge (figure 14(3a)). Corresponding $q(\rho, t)$ profiles are plotted on the rightmost column of figure 14.

Case number 1, with peaked $J_{\phi}(\rho, t)$, exhibits a monotonically increasing $q(\rho, t)$ profile, with a positive magnetic shear, growing steadily as we approach the LCFS (for a safety factor at $\bar{\psi} = 0.95$, $q_{95} \approx 10$). The $q(\rho, t)$ profile for the shot with a more uniform current distribution is plotted in figure 14(2b). After a brief initial transient, $q(\rho, t)$ assumes a relatively flat configuration with $q \approx 1.5$ from the core up to $\bar{\psi} \approx 0.65$ and $q_{95} \approx 7$. Finally, the $q(\rho, t)$ profile for instance number 3 shows a more complicated time evolution. In the time interval $t = 1 - 7$ ms, the profile exhibits a minimum around $\rho \approx 0.8$ which shifts outwards in time, and a remarkably high safety factor on the magnetic axis, $q_0 > 3$. The shape of $q(\rho, t)$ changes significantly between $t = 7$ and 8 ms, when q_0 drops to ~ 2 . Such abrupt transition is visible also in figure 14(3a) and increases substantially the internal inductance of the plasma for $t > 7$ ms.

Since the TS acquisition time is the same for shots 21 284, 21 119, and 22 289, i.e. $t_{\text{TS}} = 5$ ms, we can compare $T_e(\rho, t_{\text{TS}})$ profiles and ohmic heating density profiles, $p_{\Omega}(\rho, t_{\text{TS}})$ as done in figures 15(a) and (b), respectively. In panel (a), full dots are the actual TS measurement in each shot while shaded regions show the area within error bars on the best fits. The $T_e(\rho, t_{\text{TS}})$ profile for the high ℓ_i case (black) peaks in the plasma core slightly above $T_e = 400$ eV, keeping a relatively low edge electron temperature (at the 900 mm TS point), below $T_e = 100$ eV. The corresponding $p_{\Omega}(\rho, t_{\text{TS}})$ profile (black in figure 15(b)) produces a total ohmic heating of $P_{\Omega}(t_{\text{TS}}) \approx 0.245 \pm 0.045$ MW, when the plasma volume is $V_{\text{pl}}(t_{\text{TS}}) \approx 2.7$ m³. The $T_e(\rho, t)$ profile fit for shot 21 119 (red in figure 15) shows a parabolic trend, with core temperature slightly exceeding $T_e = 300$ eV and TS T_e at 900 mm on the order of $T_e = 150$ eV. The corresponding $p_{\Omega}(\rho, t)$ profile in figure 15(b) peaks around $\rho = 0.6$, and produces a total ohmic heating of $P_{\Omega}(t_{\text{TS}}) \approx 0.815 \pm 0.100$ MW for the 3.1 m³ plasma observed in shot 21 119 at t_{TS} . Finally a flat $T_e(\rho, t)$ is measured in shot 22 289 (blue in figure 15), which, together with the $J_{\phi}(\rho, t)$ profile at t_{TS} , is responsible for a similarly hollow ohmic heating distribution accounting for a total power $P_{\Omega}(t_{\text{TS}}) \approx 2.160 \pm 0.458$ MW in the 3.45 m³ enclosed within the LCFS. We highlight here that even if the analytical expression of the fit function, in equation (14), forces $T_e(\rho, t)$ to zero at the plasma edge, it is still able to capture

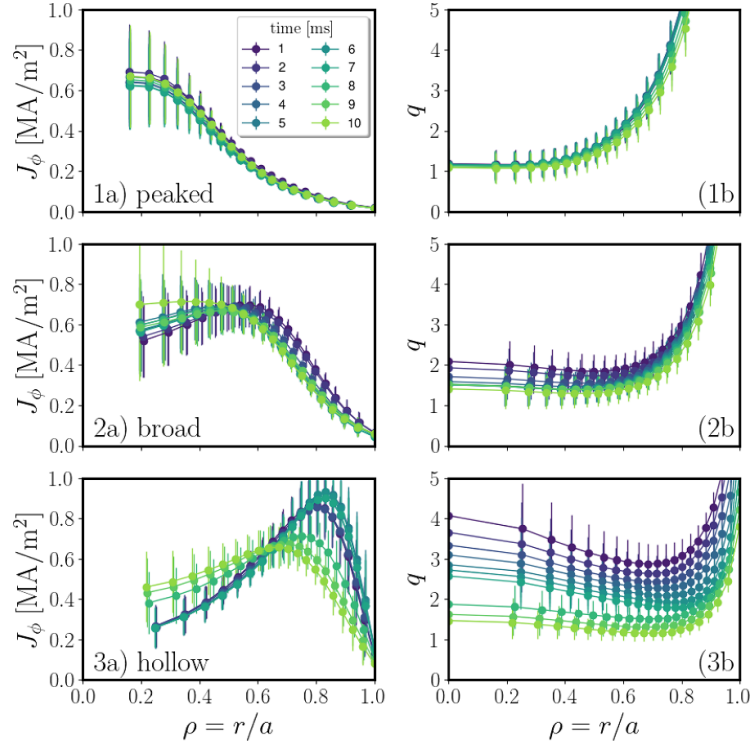


Figure 14. Profiles of (left) toroidal current density, $J_\phi(\rho, t)$, and (right) safety factor, $q(\rho, t)$, in $t = 1 - 10$ ms for shots (1a,b) 21 284, (2a,b) 21 119, and (3a,b) 22 289.

Table 3. Relevant parameters for shots 21 284, 21 119, 22 289, labeled 1, 2, and 3 in the map in figure 13. The rightmost column lists values for shot 21 100, used in section 4. Quantities in the bottom four rows are assessed at $t_{TS} = 5$ ms.

Quantity	Units	21 284	21 119	22 289	21 100
Label in figure 13	—	1	2	3	—
Formation setpoint	kV	17	22	22	22
Sustain setpoint	kV	7	7	0	7
Shots since lithium coating	—	2	29	5	12
Internal inductance, ℓ_i	—	1.357	0.870	0.410	0.779
Φ_{pl}/Φ_{vac}	—	0.011	0.041	0.137	0.047
Plasma volume, V_{pl}	m ³	2.72	3.15	3.45	3.20
Ohmic power, P_Ω	MW	0.245	0.815	2.160	0.868

fully different trends of the TS T_e measurements such as those reported in figure 15(a). Additionally, the approach adopted to assess error-bars on the fit consistently increases the uncertainty at the plasma edge for flat TS T_e profiles.

In order to highlight additional properties of the three categories of shots, relevant in the following discussion about the energy confinement time, we close the sub-section comparing time-traces of (a) shaft current $I_{sh}(t)$, (b) plasma current $I_{pl}(t)$, (c) core IF electron density IF221 $\bar{n}_e(t)$, and (d) AXUV $\bar{T}_e(t)$, in figure 16. The effect of the sustain capacitor bank on the shaft current is illustrated in figure 16(a), where the blue time-trace, for not sustained shot 22 289, drops faster than the other two curves. Shot 22 289 exhibits high I_{pl} , core IF around $\bar{n}_e = 3 \times 10^{19} \text{ m}^{-3}$, and \bar{T}_e up to 200 eV up to $t \approx 7.5$ ms, when a disruptive event induces a sudden and considerable loss of plasma thermal energy. Similar \bar{n}_e and \bar{T}_e with lower plasma current are measured in shot 21 119 (red traces in figure 16),

where the thermal energy remains roughly constant in the time lapse observed. Finally, shot 21 284, with high ℓ_i , exhibits low I_{pl} and \bar{n}_e , and a high AXUV \bar{T}_e .

5.2. Energy confinement time and effect of lithium coating

In the previous sub-section, we identified three regions in the parameter space defined by ℓ_i and Φ_{pl}/Φ_{vac} and presented examples of shots belonging to each category. For the study of the energy confinement time, τ_E , however, we will focus on the set of shots similar to 21 119 (labeled 2 in figure 13), with broad toroidal current density profiles. These plasmas are less prone to disruptive events, confine high thermal energy, up to $E_{th} \approx 8 - 9$ kJ, and are preferentially obtained with high formation setpoint and sustain at 7 kV. Shots like 21 284, with $J_\phi(\rho, t)$ profiles peaked on the magnetic axis, may attain $\tau_E \approx 5 - 7$ ms combining a very low $E_{th} < 3$ kJ and a relatively low

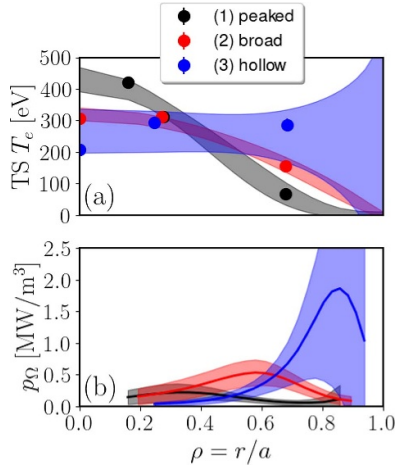


Figure 15. (a) TS $T_e(\rho, t)$ and (b) $p_\Omega(\rho, t)$ profiles for shots (black) 21 284, (red) 21 119, (blue) 22 289 at $t_{TS} = 5$ ms.

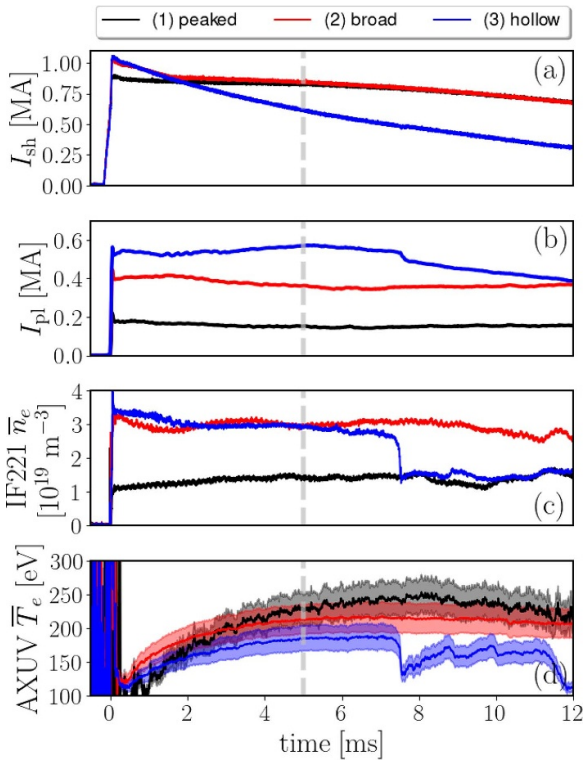


Figure 16. Time-traces of (a) shaft current $I_{sh}(t)$, (b) plasma current $I_{pl}(t)$, (c) core interferometer chord average electron density $\bar{n}_e(t)$, and (d) AXUV $\bar{T}_e(t)$ for shots (black) 21 284, (red) 21 119, and (blue) 22 289 from $t = -0.5$ to 12 ms. The formation capacitor bank is fired at $t = 0$. The dashed vertical line shows the TS acquisition time, $t_{TS} = 5$ ms.

P_Ω . At the same time, hollow $J_\phi(\rho, t)$ profiles observed in shots of the kind of 22 289 (see figures 14(3a) and (b)) can easily become unstable and trigger disruptive crashes which severely degrade the thermal energy in the plasma.

In this sub-section, we consider a dataset of 244 shots with sustain voltage 7 kV, formation setpoint ≥ 20 kV, and with varying age of lithium coating (spanning from 0 to 89 shots since last coating). Before discussing the energy confinement

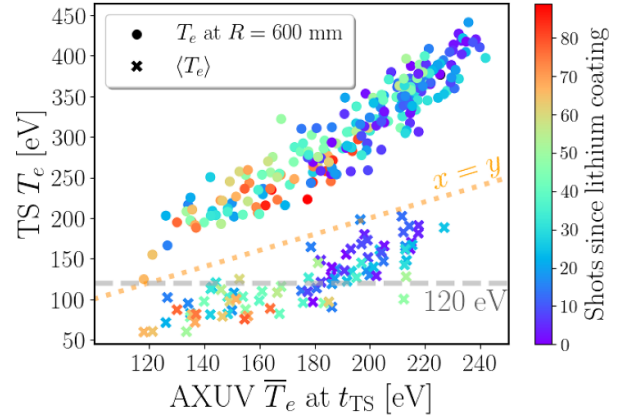


Figure 17. TS T_e at $R = 600$ mm and $\langle T_e \rangle$ versus AXUV $\bar{T}_e(t_{TS})$ at $t_{TS} = 5$ ms for each shot. The colormap shows the number of shots since lithium coating, while the dotted and the dashed lines show the curve $x = y$ for reference and TS $T_e = 120$ eV, respectively.

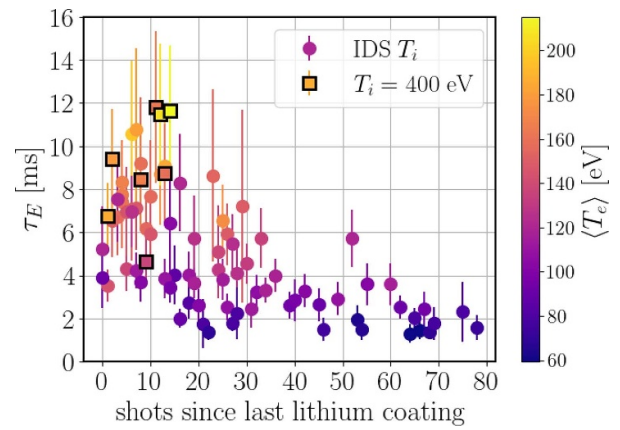


Figure 18. Energy confinement time, τ_E , at $t = t_{TS} = 5$ ms as a function of the number of shots since last lithium coating, with color scheme showing $\langle T_e \rangle$. Squares show shots with $T_i = 400 \pm 150$ eV.

time dataset, we present the variation of electron temperature with age of lithium coating, with the help of figure 17. Here, TS core T_e at $R = 600$ mm, and $\langle T_e \rangle$ are plotted as dots and crosses, respectively, against AXUV $\bar{T}_e(t_{TS})$, with $t_{TS} = 5$ ms for all 244 shots included. Note how $\langle T_e \rangle$ is available only for 101 shots in the dataset and it is missing for shots with the hottest plasma core (top right corner of figure 17). In these experiments, indeed, only the core TS T_e was measured, which did not provide enough information to compute $\langle T_e \rangle$ from a radial profile. It is possible, however, based on the trend of $\langle T_e \rangle$ for AXUV $180 < \bar{T}_e < 230$ eV, that $\langle T_e \rangle$ would keep growing for AXUV $\bar{T}_e > 230$ eV, following the increase in the core TS T_e . Both core TS T_e and $\langle T_e \rangle$ drop with number of shots since the last lithium coating, shown in the color-bar. More specifically, $\langle T_e \rangle > 120$ eV only for experiments with 20–25 shots since the last lithium coating.

The variation of τ_E with the age of the lithium coating is presented in figure 18, where the color-scheme shows $\langle T_e \rangle$ for a set of 97 sustained (7 kV) shots, and formation setpoint ≥ 20 kV, extracted from the dataset shown in figure 17. Within this group, IDS T_i is not available for a small set of 8 shots

performed with fresh lithium, for which we, then, assume a constant $T_i = 400 \pm 150$ eV in the time interval around the TS acquisition time, $t = 4 - 6$ ms. The assumption $T_i = 400$ eV follows from the mean IDS T_i observed in shots performed with similar settings. In figure 18, τ_E computed with IDS T_i and with the assumption $T_i = 400 \pm 150$ eV are plotted as dots and squares, respectively. For old lithium coatings, we observe $\tau_E \approx 1 - 2$ ms. As we reduce the age of the lithium on wall, however, shots with longer τ_E are observed. Highest values of τ_E are visible below 15–20 shots from the last lithium coating, where high $\langle T_e \rangle$ appears to play a crucial role to push the dataset above $\tau_E = 10$ ms.

6. Discussion

Toroidal current density profiles provide essential information to quantify the distribution of ohmic power in the plasma and to investigate the nature of MHD instabilities. Profiles of $J_\phi(\rho, t)$, computed with equation (18), allow to classify PI3 experiments in three categories: plasmas with peaked, broad, and hollow $J_\phi(\rho, t)$ profile.

As shown in figure 13 (for $t = 5$ ms), the shape of the current density profile changes with the amount of toroidal magnetic flux in the flux conserver, produced by the shaft current and by the poloidal plasma current. The amount and the decay rate of the vacuum toroidal flux, Φ_{vac} , are mainly determined by the setpoints of the formation and the sustain capacitor banks, while the toroidal flux produced by the plasma, Φ_{pl} , becomes significant only in shots with free decay of the shaft current, when substantial poloidal current is driven in the plasma. Low values of $\Phi_{\text{pl}}/\Phi_{\text{vac}}$ are predominantly associated with peaked $J_\phi(\rho, t)$ profiles and high internal inductance, $\ell_i > 1$. These cases exhibit $T_e(\rho, t)$ profiles peaked on the magnetic axis and low electron density compared to the other categories, yielding a total thermal energy $E_{\text{th}} \sim 2 - 3$ kJ. Additionally, the limited amount of current, mainly flowing in the hot and highly conductive plasma core, produces a low ohmic power, in the order of a few hundred kW. The current profile becomes broader and, eventually, hollow as the flux ratio is increased up to $\Phi_{\text{pl}}/\Phi_{\text{vac}} \approx 0.18$. This last class of experiments exhibits disruptive MHD activity within the first 10 ms of the plasma life, potentially responsible for a magnetic reorganization and a substantial loss of thermal energy. A possible mechanism to explain these events is current penetration [27, 46]. Here, enhanced heat and particle transport are induced by magnetic reconnection of two radially separated chains of magnetic islands produced by non-monotonic $q(\rho, t)$ profiles, such as those shown in figure 14(3b) before $t = 8$ ms.

Plasmas with broad $J_\phi(\rho, t)$ profile combine the highest thermal confinement times for PI3 with remarkable MHD stability, as shown by the time evolution of $q(\rho, t)$ in figure 14(2b), and may thus offer the best candidates for plasma compression. Together with the capacitor bank setpoints, other parameters such as the age of lithium coating, the timing and the width of the gas puff, and the current in the formation coils affect the time evolution of $J_\phi(\rho, t)$. While the gas puff and the coil currents seem to play a minor role and

will then be investigated in detail elsewhere, here we discuss the effect of lithium on PI3 plasma performance.

The beneficial effects of lithium on tokamak plasmas have been extensively investigated in the last decades on several experimental facilities [47, 48]. Lithium is an alkaline metal with high affinity for hydrogen isotopes, carbon, and oxygen. When coated on the walls on fusion plasma devices, it can retain impurities in the walls and reduce recycle of cold hydrogen fuel into the plasma. The mechanism was modeled theoretically by [49], who show that suppression of wall recycling leads to an increase in the edge plasma temperature, with consequent reduction in heat transport from the plasma core driven by strong temperature gradients. First evidence of improved plasma confinement in combination with a drop in the level of impurities in the plasma after lithium coating was reported by TFTR [50], and was attributed to a reduction in recycling of cold gas from the walls. Flattening of the electron temperature profile, with $T_e > 200$ eV at the plasma edge, after fresh lithium evaporative coating was observed in LTX [51–53] in connection with high levels of hydrogen retention in the wall.

The effect of lithium on PI3 plasmas is presented in section 5.2, where we consider a dataset of sustained shots, with high formation setpoint (≥ 20 kV), similar formation coil currents, and age of the lithium layer ranging from 0 to 89 shots since last coating. In PI3 experiments, $\langle T_e \rangle$ drops as the lithium coating degrades. In ohmically heated plasmas, high $\langle T_e \rangle$ is crucial in order to improve energy confinement because it not only contributes to increase the total plasma thermal energy, but it also prompts a reduction of the plasma resistivity and, thus, of the total ohmic dissipation. Consistently, we observe in figure 18 that highest τ_E is obtained for $\langle T_e \rangle > 120$ eV. It is, however, crucial to observe that the work presented in section 5.1, and more specifically in figure 15, suggests that flattening of $T_e(\rho, t)$ is caused by strong ohmic heating at the plasma edge when current density profiles are broad or hollow, and not by the direct action of fresh lithium. Nonetheless, retention of impurities in a fresh lithium layer would reduce the plasma resistivity and the ohmic dissipation at the edge, allowing broad $J_\phi(\rho, t)$ profiles to survive longer. As the lithium coating gets older, shots performed with sustained shaft current (i.e. $dI_{\text{sh}}/dt \sim 0$), exhibit a substantial increase in ℓ_i during the plasma lifetime, potentially due to rapid dissipation of current in the highly resistive edge region. When the sustain capacitor bank is not employed, however, plasma current driven by the rapid reduction of the vacuum toroidal flux maintains $\ell_i < 0.8$.

Currently, the PI3 diagnostic suite does not allow to assess accurately variations of the electron density at the plasma edge. However, a reflectometer system was recently installed on PI3 to monitor the evolution of the edge density profiles, and can potentially contribute to quantify the effect of lithium coating in future experimental campaigns.

As shown in figure 18, τ_E above 10 ms are obtained following the approach outlined in section 4 for sustained shots with high formation setpoint and fresh lithium coating. Furthermore, figure 17 shows that high core T_e , above 400 eV, were measured in a set of PI3 experiments where TS points at 747 and 900 mm were not available, thus preventing the

possibility of assessing $\langle T_e \rangle$ and, consequently, τ_E . This set of high core T_e was performed on a fresh lithium with PI3 control parameters similar to shots with broad $J_\phi(\rho, t)$ profile such as number 21 119 (see table 3) and shot 21 100, presented in section 4. For example, shots 20 506 and 20 508, with core $T_e \approx 438$ and 400 eV, respectively, at $t = 5$ ms, were performed with high formation setpoint (22 kV), and sustain setpoint at 7 kV. It is, then, plausible that plasmas produced in this campaign could exceed $\tau_E = 10$ ms as well.

The model described in section 4 presents, however, a number of significant limitations that will require our attention in the future in order to improve our approach to compute τ_E .

First of all, IDS measurements routinely show high T_i in the initial phase of the experiment (see figure 9) consistent with the significant ion heating expected during the bubble-burst event in CHI-formed plasmas [4, 5, 54], potentially induced by the reconnection process [55]. However, since IDS may underestimate the core T_i if carbon impurities are predominantly ionized in the core, cooling of the ion population in the core and equilibration with the electron species may be slower than the time scale measured by IDS. In this circumstance, not only would IDS report T_i from a region colder than the core, but it also would prevent us from computing the heating power flowing from the hot ion population into the electrons accurately. A supplementary technique to improve measurements of core T_i in PI3 based on neutron counters is currently under development. Once available and used in combination with IDS, it will allow us to understand more thoroughly the ion dynamics in PI3 plasma.

Second, characterizing the species and the distribution of impurities is crucial to describe the power balance in the plasma accurately. On the one hand, knowledge of the plasma composition is necessary to estimate the resistivity of the plasma via the factor $f_i(Z_{\text{eff}})$ in equation (8). The assumption adopted in this work, $Z_{\text{eff}}(\rho, t) = Z_{\text{eff}} = 2 \pm 1$, is obtained as average of the expected amount of impurities in shots with fresh and with old lithium coating. In the first case, low recycling of impurities from the wall could maintain the plasma clean, with Z_{eff} slightly above 1. In the second scenario, we expect higher concentration of impurities in the plasmas and assume Z_{eff} to grow up to the $Z_{\text{eff}} = 3$. Note that the ohmic power density profiles in figure 15(b) may be perturbed by non-homogeneous distributions of impurities in the plasma. On the other hand, impurities must be taken into account in the calculation of E_{th} , equation (6), where the average ion charge, Z_{ave} , is introduced to quantify the dilution of the deuterium plasma. Abundance of impurities in the plasma is, thus, doubly detrimental for energy confinement because it reduces the amount of E_{th} in the deuterium species and promotes dissipation of plasma current through ohmic power. Work on PI3 diagnostics to measure Z_{eff} based on a survey spectrometer and on a filterscope collecting bremsstrahlung radiation at $\lambda = 523$ nm is already ongoing.

Finally, the model neglects the ohmic heating produced by the poloidal plasma current. Equilibrium reconstruction suggests that the fraction of total P_Ω due to the poloidal current would not exceed 10% of the total power, and would then be comparable to the contribution predicted from the bootstrap current in section 3. However, both assessments rely on preliminary calculations and require additional effort and analysis to confirm the result.

7. Conclusions

We have constructed an approach to characterize the thermal energy confinement time, τ_E , of spherical tokamak plasmas formed in the PI3 device without the use of a diamagnetic loop voltage. The thermal energy confinement time is the ratio between the total thermal energy in the plasma and the difference between the ohmic power and the time derivative of the thermal energy. We have obtained the total plasma thermal energy by use of temperature and density diagnostics combined data from a plasma equilibrium reconstruction algorithm. Assessing the ohmic heating in the plasma has required a novel method. We compute the ohmic heating from a profile of toroidal plasma current generated by equilibrium reconstruction and an estimate of the profile of the plasma resistivity. The time derivative of the total plasma thermal energy is obtained by leveraging the high time resolution of the AXUV diagnostic. A number of additional assumptions and approximations have been required, in particular an assumption of the functional form of the one-dimensional radial profiles of electron density, electron temperature, and ion temperature. The uncertainty in the ion temperature distribution and the plasma impurity abundances (and $Z_{\text{eff}}, Z_{\text{avg}}$) are significant contributors to the overall uncertainty in τ_E .

We have implemented these procedures along with Monte Carlo uncertainty analysis. On characterizing the plasma current profiles of a wide range of PI3 shots, we determined that the plasmas follow a trend determined by machine settings, and can be grouped into three classes with different characteristics by the shape of the current profile, electron temperature profile, the ohmic power density profile. We have presented results for the set of PI3 shots with broad current profiles which exhibit the best thermal confinement properties and MHD stability. The best results in terms of energy confinement are obtained with sustained shaft current and fresh lithium coating of the PI3 walls. Notably, the best energy confinement times also correspond to the hottest volume average electron temperatures. This is consistent with an expectation that at higher temperatures the same plasma current produces less ohmic heating, and the plasma's total thermal energy is also higher. We find PI3 plasmas at 5 ms into the discharge can have thermal confinement times in excess of 10 ms.

These results demonstrate that by forming meter-scale plasmas, we can obtain thermal confinement times which

can achieve significant heating if compressed on millisecond timescales. A practical manner of achieving this at the meter scale is by the use of a electromagnetic compression system using theta-pinch coils. It has previously been established that a plasma q -profile can be selected to maintain plasma stability during compression [56, 57], as would be required to maintain good thermal confinement. This will allow the next step past the PCS-16 device [20] in demonstrating the practicality of MTF.

Acknowledgment

The authors thank Ivan Khalzov, Martin Cox, and Kurt Schoenberg for the insightful discussion and constructive comments. This work was supported by funding from the Government of Canada through its Strategic Innovation Fund (Agreement No. 811-811346). The funding source had no involvement in: the study design; the collection, analysis and interpretation of data; the writing of the report; the decision to submit the article for publication.

Appendix. Rationale for the assumptions on Z_{ave} and Z_{eff}

The definitions of the average and of the effective ion charge are

$$Z_{\text{ave}} = \frac{n_e}{\sum_s n_s}, \quad (\text{A.1})$$

$$Z_{\text{eff}} = \frac{\sum_s Z_s^2 n_s}{\sum_s Z_s n_s} = \frac{\sum_s Z_s^2 n_s}{n_e}, \quad (\text{A.2})$$

respectively, where n_e is the electron density, n_s is the density of the s th ion species, and Z_s is the charge state of the s th ion species. The assumptions

$$Z_{\text{ave}} = 1.5 \pm 0.5, \quad (\text{A.3})$$

$$Z_{\text{eff}} = 2 \pm 1, \quad (\text{A.4})$$

adopted in the manuscript follow from the study of the single impurity case, where we assume that the plasma contains only one additional ion species beside deuterium. In this case, equations (A.1) and (A.2) can be simplified as

$$Z_{\text{ave}} = \frac{1 + xZ}{1 + x}, \quad (\text{A.5})$$

$$Z_{\text{eff}} = \frac{1 + xZ^2}{1 + xZ}, \quad (\text{A.6})$$

where $x = n_i/n_d$ with n_i and n_d number density of the impurity and of the deuterium population, respectively, and Z charge state of the single impurity species. Contour plots of the expressions in equations (A.5) and (A.6) are shown in the left and in the right panel of figure A1, respectively. Here, blue-shaded areas show the regions corresponding to the assumptions in equations (A.3) and (A.4), while red dashed lines show the charge state corresponding to fully ionized lithium, $Z = 3$.

In order to explain the rationale behind equations (A.3) and (A.4), we consider two scenarios: the case of plasmas produced after lithium coating the PI3 walls and the case of plasmas injected in a flux conserver with an old and worn lithium coating.

Immediately after coating (the first scenario), low recycling due to lithium should reduce the inflow of impurities from the wall into the plasma and maintain the fraction of carbon and oxygen in the plasma at negligible levels. In this case, we assume that lithium is the dominant impurity in the plasma and since the PI3 TS system measures T_e larger than the third ionization energy of lithium, $E_{\text{Li},3} \approx 120 \text{ eV}$, we must consider all possible charge states of lithium, $Z = 1$ to $Z = 3$. For $Z = 3$, we can observe in figure A1 (left) that at $n_{\text{Li}} = n_d$ (which is $x = 1$) we have $Z_{\text{ave}} = 2$. Equation (A.3) then allows us to include in the model all possible scenarios with lithium as a dominant impurity, for $x \in [0, 1]$.

When the lithium layer is worn out (the second scenario), carbon, nitrogen, and oxygen are assumed to be the dominant impurity populations in the plasma, with a charge state $Z = 6$ to $Z = 8$ for $T_e \lesssim 450 \text{ eV}$ [30]. In this range of Z , the assumption $Z_{\text{ave}} = 2$ returns values of the impurity concentration in the range $x \in [0.2, 0.25]$, which may be a realistic upper bound for the impurity concentration.

So thanks to the shape of the $Z_{\text{ave}} = 2$ curve, the assumption in equation (A.3) allows one to simultaneously describe plasmas with abundant low- Z impurities, such as lithium, and plasmas with smaller concentrations of impurities with higher charge state such as carbon, nitrogen, and oxygen.

The assumption for Z_{eff} in equation (A.4) was adopted to select a region of the x - Z space similar to the area under the curve $Z_{\text{ave}} = 2$.

Finally, PI3 plasmas may also contain traces of tungsten and silver eroded from the electrodes of the Marshall gun and aluminum from the flux conserver.

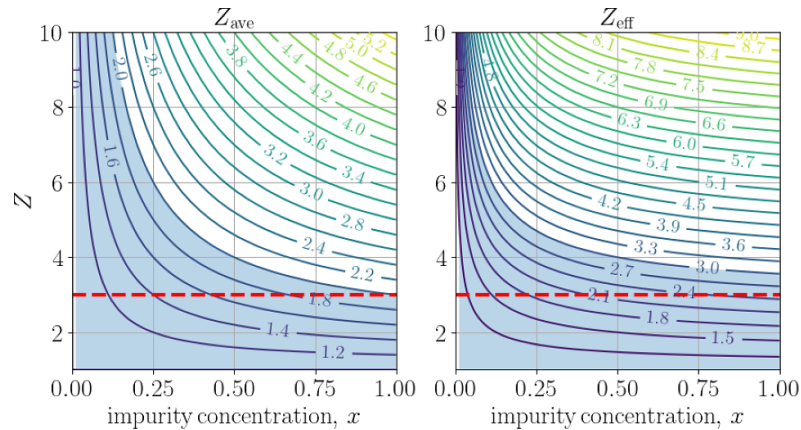


Figure A1. Contour plot of (left) Z_{ave} and (right) Z_{eff} for a single impurity as a function of the impurity charge state, Z , and of the impurity concentration $x = n_i/n_d$.

The concentration of these impurities is however expected to be sufficiently low as to be neglected in our model.

ORCID iDs

A. Tancetti [ID https://orcid.org/0000-0002-8048-007X](https://orcid.org/0000-0002-8048-007X)
 C. Ribeiro [ID https://orcid.org/0000-0003-0361-8554](https://orcid.org/0000-0003-0361-8554)
 S. Coop [ID https://orcid.org/0000-0003-1538-3940](https://orcid.org/0000-0003-1538-3940)
 C.P. McNally [ID https://orcid.org/0000-0002-2565-6626](https://orcid.org/0000-0002-2565-6626)
 M. Reynolds [ID https://orcid.org/0000-0001-5880-2290](https://orcid.org/0000-0001-5880-2290)
 X. Feng [ID https://orcid.org/0000-0001-5981-914X](https://orcid.org/0000-0001-5981-914X)
 A. Rohollahi [ID https://orcid.org/0000-0001-6688-8696](https://orcid.org/0000-0001-6688-8696)
 C. Dunlea [ID https://orcid.org/0000-0002-9464-0599](https://orcid.org/0000-0002-9464-0599)

References

- [1] Turchi P.J., Cooper A.L., Ford R.D., Jenkins D.J. and Burton R.L. 1980 *Review of the NRL Liner Implosion Program* (Springer) pp 375–86
- [2] Siemon R.E., Lindemuth I.R. and Schoenberg K.F. 2021 Why magnetized target fusion offers a low-cost development path for fusion energy *Plasma Phys. Control. Fusion*. **18** 363
- [3] Laberge M. 2019 Magnetized target fusion with a spherical tokamak *J. Fusion Energy* **38** 199–203
- [4] Bellan P.M. 2000 *Spheromaks: a Practical Application of Magnetohydrodynamic Dynamos and Plasma Self-Organization* (World Scientific)
- [5] Auerbach D., Hill D.N. and McLean H.S. 2001 Ion temperature measurements in sspX *Undergraduate Thesis* Swarthmore College
- [6] Marshall J. 1960 Performance of a hydromagnetic plasma gun *Phys. Fluids* **3** 134–5
- [7] Nelson B.A., Jarboe T.R., Orvis D.J., McCullough L.A., Xie J., Zhang C. and Zhou L. 1994 Formation and sustainment of a 150 kA tokamak by coaxial helicity injection *Phys. Rev. Lett.* **72** 3666–9
- [8] Jarboe T.R., Bohnet M.A., Mattick A.T., Nelson B.A. and Orvis D.J. 1998 Results from current drive experiments on the Helicity Injected Torus *Phys. Plasmas* **5** 1807–14
- [9] Redd A.J., Nelson B.A., Jarboe T.R., Gu P., Raman R., Smith R.J. and McCollam K.J. 2002 Current drive experiments in the helicity injected torus (HIT-II) *Phys. Plasmas* **9** 2006–13
- [10] Nagata M., Kanki T., Fukumoto N. and Uyama T. 2003 The internal magnetic field structures and current density profiles in the helicity injected spherical torus plasma driven by coaxial helicity injection *Phys. Plasmas* **10** 2932–9
- [11] Browning P.K., Cunningham G., Duck R., Gee S.J., Gibson K.J., Kitson D.A., Martin R. and Rusbridge M.G. 1992 Injection and sustainment of plasma in a preexisting toroidal field using a coaxial helicity source *Phys. Rev. Lett.* **68** 1722–5
- [12] Shimamura S., Taniguchi M., Takahashi T. and Nogi Y. 1995 Formation and sustainment of a low aspect ratio tokamak by a series of plasma injections *Fusion Technol.* **27** 361–4
- [13] Yamada M., Ono Y., Hayakawa A., Katsurai M. and Perkins F.W. 1990 Magnetic reconnection of plasma toroids with cohelicity and counterhelicity *Phys. Rev. Lett.* **65** 721–4
- [14] Carle P.J.F., Howard S. and Morelli J. 2013 High-bandwidth polarimeter for a high density, accelerated spheromak *Rev. Sci. Instrum.* **84** 307
- [15] Carle P., Froese A., Wong A., Howard S., O’Shea P. and Laberge M. 2016 Polarimeter for the general fusion spectrometer machine *Rev. Sci. Instrum.* **87** 797
- [16] Young W.C. and Parfeniuk D. 2016 Thomson scattering at general fusion *Rev. Sci. Instrum.* **87** 915
- [17] Raman R. et al 2007 Non-inductive solenoid-less plasma current startup in NSTX using transient CHI *Nucl. Fusion* **47** 792
- [18] Raman R. and Shevchenko V.F. 2014 Solenoid-free plasma start-up in spherical tokamaks *Plasma Phys. Control. Fusion* **56** 103001
- [19] Kuroda K. et al 2023 Demonstration of transient CHI startup using a floating biased electrode configuration *Nucl. Fusion* **64** 014002
- [20] Howard S.J. et al 2024 Measurement of spherical tokamak plasma compression in the pcs-16 magnetized target fusion experiment *Nucl. Fusion* **65** 016029
- [21] Rohollahi A., Elgriw S., Mossman A., Adegun J., Bsharat H., Voldiner I. and Xiao C. 2019 Effects of lithium coating of the chamber wall on the STOR-M tokamak discharges *Nucl. Fusion* **59** 076023
- [22] Semenov I., Mirnov S., Darrow D., Roquemore L., Fredrickson E.D., Menard J., Stutman D. and Belov A. 2003 Phenomenology of internal reconnections in the national spherical torus experiment *Phys. Plasmas* **10** 664–70
- [23] Howard S.J., Horton R.D., Hwang D.Q., Evans R.W. and Brockington S.J. 2008 Calibration of magnetic probes in the vicinity of a conducting well *Rev. Sci. Instrum.* **79** 023503

- [24] Braglia F.G., Gutjahr C., Bolanos S. and Ahmed M. 2022 Improved magnetic diagnostics on general fusion plasma injector 3 *Bull. Am. Phys. Soc.* **67** U11.008
- [25] Meeker D. 2013 Finite element method magnetics, version 4.2 user's manual (available at: www.femm.info/wiki/manual)
- [26] Hossack A.C., Morgan K.D., Hansen C.J. and Sutherland D.A. 2022 A multi-chord, two-color interferometer using Hilbert transform phase detection for measuring electron density in spheromak plasmas *Rev. Sci. Instrum.* **93** 093501
- [27] Wesson J. and Campbell D.J. 2011 *Tokamaks (International Series of Monographs in Physics)* vol 149 (Oxford University Press)
- [28] Huba J.D. 2011 *NRL Plasma Formulary* (United States Naval Research Laboratory)
- [29] Fung J. 2006 High resolution flow and ion temperature measurements with ion Doppler spectroscopy at SSX *Bachelor's Thesis* Swathmore (available at: <https://works.swarthmore.edu/theses/702>)
- [30] Edmund Post D.E., Jensen R.V., Tarter C.B., Grasberger W.H. and Lokke W.A. 1977 Steady-state radiative cooling rates for low-density, high-temperature plasmas *At. Data Nucl. Data Tables* **20** 397–439
- [31] Baião D. *et al* 2012 Central electron temperature estimations of TJ-II neutral beam injection heated plasmas based on the soft x ray multi-foil technique *Rev. Sci. Instrum.* **83** 053501
- [32] Scannell R. *et al* 2008 Design of a new Nd:YAG Thomson scattering system for MAST *Rev. Sci. Instrum.* **79** 10E730
- [33] Fischer R., Wendland C., Dinklage A., Gori S. and Dose V. the W7-AS Team 2002 Thomson scattering analysis with the Bayesian probability theory *Plasma Phys. Control. Fusion* **44** 1501
- [34] Selden A.C. 1980 Simple analytic form of the relativistic Thomson scattering spectrum *Phys. Lett. A* **79** 405–6
- [35] Froese A. *et al* 2022 Bayesian equilibrium reconstruction for general fusion demonstration plant *Bull. Am. Phys. Soc.* **67** BP11.003
- [36] Grad H. and Rubin H. 1958 Hydromagnetic equilibria and force-free fields *J. Nucl. Energy* **7** 284–5
- [37] Papoulis A. 2002 *Probability, Random Variables and Stochastic Processes* (McGraw-Hill)
- [38] Bartlett D.V. *et al* 1988 Energy confinement in jet ohmically heated plasmas *Nucl. Fusion* **28** 73
- [39] Nagami M. *et al* 1982 Energy confinement of ohmically heated d-shaped plasmas in doublet iii *Nucl. Fusion* **22** 3
- [40] Kessel C.E. 1994 Bootstrap current in a tokamak *Nucl. Fusion* **34** 1221–38
- [41] Sauter O., Angioni C. and Lin-Liu Y.R. 1999 Neoclassical conductivity and bootstrap current formulas for general axisymmetric equilibria and arbitrary collisionality regime *Phys. Plasmas* **6** 2834–9
- [42] Virtanen P. *et al* (SciPy 1.0 Contributors) 2020 SciPy 1.0: fundamental algorithms for scientific computing in Python *Nat. Methods* **17** 261–72
- [43] Lee M.W., Lim S., Jeong W., Kim S., Kim J.H., Hwang Y.S. and Sung C. 2023 Electron temperature measurements using a two-filter soft x-ray array in vest *Sensors* **23** 8357
- [44] Delgado-Aparicio L.F., Stutman D., Tritz K., Finkenthal M., Bell R., Hosea J., Kaita R., LeBlanc B., Roquemore L. and Wilson J.R. 2007 Fast electron temperature measurements using a 'multicolor' optical soft x-ray array *J. Appl. Phys.* **102** 34
- [45] Heng L.A.N. *et al* 2017 Analysis of electron temperature, impurity transport and mhd activity with multi-energy soft x-ray diagnostic in east tokamak *Plasma Sci. Technol.* **19** 125101
- [46] Stix T.H. 1976 Current penetration and plasma disruption *Phys. Rev. Lett.* **36** 521
- [47] Ono M. 2012 Lithium as plasma facing component for magnetic fusion research *Technical Report* (Princeton Plasma Physics Lab.(PPPL), Princeton, NJ (United States))
- [48] De Castro A., Moynihan C., Stemmley S., Szott M. and Ruzic D.N. 2021 Lithium, a path to make fusion energy affordable *Phys. Plasmas* **28** 050901
- [49] Krasheninnikov S.I., Zakharov L.E. and Pereverzev G.V. 2002 On lithium wall and performance of magnetic fusion device *APS Division of Plasma Physics Meeting Abstracts* vol 44 p GI1–006
- [50] Mansfield D.K. *et al* 2001 Observations concerning the injection of a lithium aerosol into the edge of tfr discharges *Nucl. Fusion* **41** 1823
- [51] Kaita R. *et al* 2010 Experiments with liquid metal walls: Status of the lithium tokamak experiment *Fusion Eng. Des.* **85** 874–81
- [52] Boyle D.P., Majeski R., Schmitt J.C., Hansen C., Kaita R., Kubota S., Lucia M. and Rognlien T.D. 2017 Observation of flat electron temperature profiles in the lithium tokamak experiment *Phys. Rev. Lett.* **119** 015001
- [53] Maan A. *et al* 2023 Improved neutral and plasma density control with increasing lithium wall coatings in the lithium tokamak experiment- β (ltx- β) *Nucl. Mater. Energy* **35** 101408
- [54] Fernández J.C., Jarboe T.R., Knox S.O., Hennis I. and Marklin G.J. 1990 Ion heating and current drive from relaxation in decaying spheromaks in mesh flux conservers *Nucl. Fusion* **30** 67
- [55] Hsu S.C., Fiksel G., Carter T.A., Ji H., Kulsrud R.M. and Yamada M. 2000 Local measurement of nonclassical ion heating during magnetic reconnection *Phys. Rev. Lett.* **84** 3859
- [56] Brennan D., Froese A., Reynolds M., Barsky S., Wang Z., Delage M. and Laberge M. 2020 Stable compression of a spherical tokamak plasma *Nucl. Fusion* **60** 046027
- [57] Brennan D., Froese A., Reynolds M., Barsky S., Wen A., Wang Z., Delage M. and Laberge M. 2021 A stable corridor for toroidal plasma compression *Nucl. Fusion* **61** 046047